HHS Public Access

Author manuscript

Nat Cell Biol. Author manuscript; available in PMC 2020 February 26.

Published in final edited form as:

Nat Cell Biol. 2019 September ; 21(9): 1113–1126. doi:10.1038/s41556-019-0373-7.

Immuno-subtyping of breast cancer reveals distinct myeloid cell profiles and immunotherapy resistance mechanisms

Ik Sun Kim[1,2,3,4], **Yang Gao**[3,4], **Thomas Welte**[1,3,4], **Hai Wang**[1,3,4], **Jun Liu**[1,3,4], **Mahnaz Janghorban**[3,4], **Kuanwei Sheng**[2,3,5], **Yichi Niu**[3,5], **Amit Goldstein**[1,3,4], **Na Zhao**[3,4], **Igor Bado**[1,3,4], **Hin-Ching Lo**[1,2,3,4], **Michael J. Toneff**[3,4,9], **Tuan Nguyen**[3,4,6], **Wen Bu**[1,3,4], **Weiyu Jiang**[1,3,4], **James Arnold**[3,7], **Franklin Gu**[3,7], **Jian He**[10], **Deborah Jebakumar**[10], **Kimberly Walker**[9], **Yi Li**[1,3,4], **Qianxing Mo**[5,11], **Thomas F. Westbrook**[3,5,7], **Chenghang Zong**[3,5,8], **Arundhati Rao**[10], **Arun Sreekumar**[3,4], **Jeffrey M. Rosen**[3,4], **Xiang H.-F. Zhang**[1,3,4,8]

[1]Lester and Sue Smith Breast Center, Baylor College of Medicine, One Baylor Plaza, Houston, TX, 77030

[2]Integrative Molecular and Biomedical Sciences Graduate Program, Baylor College of Medicine, One Baylor Plaza, Houston, TX, 77030

[3]Dan L. Duncan Cancer Center, Baylor College of Medicine, One Baylor Plaza, Houston, TX, 77030

Correspondence (Lead Contact): Xiang H.-F. Zhang, BCM600, One Baylor Plaza, Houston, TX, 77030 USA, Phone: 713-798-6239, xiangz@bcm.edu.

AUTHOR CONTRIBUTIONS

Conception and design: X.H.-F.Z., I.S.K. and J.M.R. Development of methodology: I.S.K., X.H.-F.Z., T.W., M.J.T., H.W., J.L., K.S., Y.L., Q.M., T.F.W., C.Z., A.R., and A.S. Acquisition of data: I.S.K., Y.G., T.W., M.J., N.Z., A.G., Y.N., H-C.L., I.B., T.N., W.B., W.J., J.A., F.G., J.H., D.J., K.W., and X.H.-F.Z. Analysis and interpretation of data: I.S.K., X.H.-F.Z., and J.M.R. Writing and review of manuscript: X.H.-F.Z., I.S.K., and J.M.R. Study supervision: X.H.-F.Z.

COMPETING FINANCIAL INTERESTS

The authors declare no competing financial interests.

Data Availability

The RNA-seq data for cancer cells, tumor-infiltrating macrophages, tumor-infiltrating neutrophils have been submitted to the Gene Expression Omnibus under accession number GSE104765. The normalized RNA-seq data for human TNBC nanostring datasets are provided in Supplementary Table 2c.

Other secondary datasets used in this study include:

1. TCGA dataset, available from https://portal.gdc.cancer.gov/. The sample IDs used in this study are provided in Supplementary Table 2d.
2. METABRIC dataset, available from https://ega-archive.org/datasets/EGAD00010000266.
3. BioGPS Primary Cell Atlas, available from http://biogps.org/dataset/BDS_00013/primary-cell-atlas/. The specific samples used in this study are listed in Supplementary Table 2a.
4. Gene expression profiles of TAN, GMDSC and normal neutrophils. Data available from GEO, dataset GSE43254.
5. Riaz et al., metastatic melanoma dataset: https://github.com/riazn/bms038_analysis
6. Hugo et al., metastatic melanoma dataset available from GEO: GSE78220.

Statistical Source Data of all other figures are available in Supplementary Table 5.

All other data supporting the findings of this study are available from the corresponding author on reasonable request.

Code availability

Key codes for data analyses and major intermediate data are available at Github: https://github.com/Xiang-HF-Zhang/Dichotomous-of-innate-immune-landscape.

[4]Department of Molecular and Cellular Biology, Baylor College of Medicine, One Baylor Plaza, Houston, TX, 77030

[5]Department of Molecular and Human Genetics, Baylor College of Medicine, One Baylor Plaza, Houston, TX, 77030

[6]Graduate Program in Translational Biology and Molecular Medicine, Baylor College of Medicine, One Baylor Plaza, Houston, TX, 77030

[7]Verna & Marrs McLean Department of Biochemistry and Molecular Biology, Baylor College of Medicine, One Baylor Plaza, Houston, TX, 77030

[8]McNair Medical Institute, Baylor College of Medicine, One Baylor Plaza, Houston, TX, 77030

[9]Present address: Department of Biology, Widener University, One University Place, Chester, PA 19013

[10]Scott and White Medical Center, Baylor Scott and White Healthcare, Temple, Texas, USA

[11]Present address: Department of Biostatistics & Bioinformatics, H. Lee Moffitt Cancer Center & Research Institute, Tampa, FL 33612

Abstract

Cancer-induced immune responses affect tumor progression and therapeutic response. In multiple murine models and clinical datasets, we identified large variations of neutrophils and macrophages, which define “immune subtypes” of triple negative breast cancer (TNBC) including neutrophil-enriched (NES) and macrophage-enriched subtypes (MES). Different tumor-intrinsic pathways and mutual regulation between macrophages/monocytes and neutrophils contribute to the development of dichotomous myeloid compartment. MES contains predominantly macrophages that are CCR2-dependent and exhibit variable responses to immune checkpoint blockade (ICB). NES exhibits systemic and local accumulation of immunosuppressive neutrophils (or granulocytic myeloid-derived suppressor cells (gMDSCs), is resistant to ICB, and contains a minority of macrophages that appear to be unaffected by CCR2 knockout. A MES-to-NES conversion mediated acquired ICB resistance of initially sensitive MES models. Our results demonstrate diverse myeloid cell frequencies, functionality, and potential roles in immunotherapies, and highlight the need to better understand the inter-patient heterogeneity of the myeloid compartment.

INTRODUCTION

Immune cells participate in every aspect of tumor progression[1]. Many immune cells may play disparate roles – anti-tumorigenic in some situations, pro-tumorigenic in others[2]. For instance, macrophages undergo different activation and polarization[3,4]: the classically activated subsets potentiate anti-tumor immunity[5,6] whereas the alternatively activated subsets promote tumors through multiple mechanisms[7,8]. Neutrophils also play opposing roles in different settings[9–12], probably due to plasticity and heterogeneity. Therefore, it is critical to understand how immune cell functions vary in different tumor contexts.

Solid tumors also induce systemic immune alterations[13,14]. Immature neutrophils and monocytes may accumulate in blood and immune organs, develop immunosuppressive activity, and alter tumor progression either by infiltrating tumors[11,15], or via homing to distant organs to establish pre-metastatic niches[16–18].

It remains elusive how these local and systemic immune aberrations are related to inter-tumoral heterogeneity. This has been predominantly characterized based on tumor-intrinsic features[19–21], where different subtypes of breast cancer exhibit distinct developmental programs, metastatic behaviors, and molecular landscapes[22–25].

Variations in immune profiles have been linked to prognosis, therapeutic responses, and breast cancer subtypes[26–30]. However, it remains a challenge to dissect the causal effects and mechanistic functions of different immune cells solely based on clinical data. The current study overcomes these limitations by integrating the immunological characterization of a variety of murine syngeneic mammary tumor models with the analyses of human breast cancer datasets.

RESULTS

Immune cell profiling of murine tumor models reveals a dichotomous distribution of macrophages and neutrophils

We chose eight syngeneic murine tumor models derived from either a BALB/c or C57BL/6 background, and maintained as cell lines or primary tissues (Supplementary Fig. 1a). In particular, PyMT-M and PyMT-N were derived from a same C57/BL6 tumor but exhibited different properties. MMTV-PyMT tumors express ER in early tumorigenesis but progressively lose ER as tumors develop[31]. We confirmed the lack of ER, PR, and ErbB2 expression in PyMT-M and PyMT-N tumors (Supplementary Fig. 1b, c). These and previous results[32–34] indicate that by definition the eight models represent triple-negative breast cancer (TNBC). TNBC is a heterogeneous group of diseases[21]. Expression of characteristic genes suggested that these models resemble luminal-like (2208L and PyMT-N), basal-like (4T1 and AT3), and the claudin-low (PyMT-M, E0771, and 67NR) subtypes (Supplementary Fig. 1d) – covering a spectrum of differentiation[35] and metastatic propensity (Supplementary Fig. 1e). Thus, these models may collectively represent heterogeneous TNBC.

Major immune cell populations were profiled (Supplementary Fig. 1f), when tumors reached a similar size (Supplementary Fig. 1g). Hierarchical clustering was performed to display FACS-determined cell frequencies (Supplementary Fig. 1h). We prioritized different cell types based on inter-model variations and median frequencies (Supplementary Table 1). Tumor-infiltrating neutrophils (TINs) and macrophages (TIMs) were the most frequent and variable cell types across models, as confirmed by immunofluorescence staining of Ly6G and F4/80 (Supplementary Fig. 1i).

TINs are defined by $CD45^+CD11b^+Ly6G^+Ly6C^{med\text{-}low}$, and TIMs are defined by $CD45^+CD11b^+Ly6G^{TM}Ly6C^{TM}F4/80^+$ (Fig. 1a, b). $F4/80^+$ cells are $CD64^+$[36] (Fig. 1c). Wright-Giemsa staining confirmed their “polymorphonuclear/multi-lobed” and “mononuclear” morphology, respectively (Fig. 1d).

We next extended TIM/TIN analyses to additional seven syngeneic murine and five patient-derived xenograft (PDX) TNBC models. PDXs informed residual immune cells infiltrating human tumors in SCID/Beige mice. Circulating immune cells were examined to evaluate systemic alterations. We performed unsupervised clustering using TIM, TIN, peripheral blood neutrophils (PBNs, $CD45^{+}CD11b^{+}Ly6G^{+}Ly6C^{med\text{-}low}$), monocytes (PBMs, CD45 CD11b Ly6G $Ly6C^{high}$), and total tumor-infiltrating $CD45^{+}$ cells. PBNs and PBMs are potential sources of TINs and TIMs, respectively.

Four clusters were observed (Fig. 1e), mainly driven by: 1) the total CD45+ cells and 2) the TIN/TIM ratio (Fig. 1f). PDX tumors in SCID/Beige mice mostly fell into Cluster II with low CD45+ cells. However, some PDXs were sorted to other clusters, and some murine tumors fell into Cluster II and exhibited a low T cell infiltration (Supplementary Fig. 1j), arguing against a specific link between immunodeficiency and the “cold” phenotype.

The TIN/TIM ratio is another cluster-driving factor. Clusters I and IV represent tumors with increased TINs, whereas cluster II and III represent those with increased TIMs. The TIN/TIM ratio exhibited a bimodal distribution (Fig. 1f).

The TIN frequency strongly correlated with PBNs (Fig. 1g), indicating that systemic neutrophil accumulation accompanied local TIN enrichment, which was also evidenced by splenomegaly (Supplementary Fig. 1k) and alterations in the bone marrow (Supplementary Fig. 1l). This was opposite to the weak correlations among TIMs, PBMs and tumor-infiltrating monocytes (Fig. 1h,i).

Taken together, we divided pre-clinical models into immunological cold, macrophage-enriched (MES), or neutrophil-enriched subtype (NES). MES features local accumulation of macrophages with few neutrophils and little systemic impact. In contrast, NES features local and systemic neutrophil accumulation. In NES, macrophages are still present, sometimes as frequent as neutrophils.

Provided immunosuppressive activities, $CD45^{+}CD11b^{+}Ly6G^{+}Ly6C^{med\text{-}low}$ cells in tumor-bearing hosts were also defined as granulocytic myeloid-derived suppressor cells (gMDSCs)[15,37], tumor-associated neutrophils (TANs)[11,37,38], or immunosuppressive neutrophils[39]; $CD45^{+}CD11b^{+}Ly6G^{™}Ly6C^{high}$ and $CD45^{+}CD11b^{+}Ly6G^{™}Ly6C^{™}F4/80^{+}$ cells were also termed monocytic MDSCs[8,15,37] and tumor-associated macrophages[40], respectively; together these cells were also called immature myeloid cells[41]. However, the suppressive and immature properties of neutrophils/macrophages vary widely among the models in this study. Thus, we prefer more generic terms, TIN and TIM, to describe the comparisons among various models.

Inter-tumoral variation of neutrophils and macrophages across human TNBCs

To examine TIM/TIN in human tumors, we first analyzed a TNBC dataset with matched tissue microarray (TMA) and Nanostring assays of 750 immunity-related genes. Using the human Primary Cell Atlas of BioGPS (http://biogps.org/dataset/BDS_00013/primary-cell-atlas/)[42], we identified subsets of Nanostring genes differentially expressed between macrophages and neutrophils (Fig. 2a). Thirty-three macrophage-specific genes (MSGs) and

45 neutrophil-specific genes (NSGs) were identified to cluster TNBCs (Fig. 2b). Four clusters were uncovered, ranging from MSG-enriched (right-most) to NSG-enriched (left-most) (Fig. 2b). One cluster lacks both, and may represent "cold" tumors. The expression of *Elastase* and *G-CSF*, genes highly relevant for neutrophil biology[43,44], confirmed the neutrophil variation, and *CD68* expression appears consistent with MSGs (Fig. 2b). Immunohistochemical (IHC) staining of CD68 in matched TMA revealed variable macrophage infiltration across tumors (Fig. 2b). TMA sections with strong CD68 staining (> 10 positive cells) express a higher level of MSGs (Fig. 2c), supporting the Nanostring-based analysis. Furthermore, the MSG/NSG ratio exhibited a bimodal distribution (Fig. 2d), consistent with observations in murine models.

Next, we analyzed larger datasets using CIBERSORT and TIMER[27,45] to deconvolute immune infiltration from bulk tumor transcriptomes. Hierarchical clustering of TIMER scores of six cell types revealed distinct clusters among TCGA TNBC dataset (Fig. 2e): a "cold" cluster with overall low immune infiltration, another cluster with higher infiltration of TIM and CD8+ T cells, and the rest with TIN and other immune cells. In confirmation, we conducted t-Distributed Stochastic Neighbor Embedding (tSNE) using TIMER-scores, resulting in three clusters corresponding to tumors that are cold, TIM-enriched, and TIN-enriched (Fig. 2f). Analysis of non-TNBCs in TCGA and TNBC in METABRIC[46] led to similar results (Supplementary Fig. 2a–c). We next analyzed CIBERSORT outputs of >1000 TNBC[47] (Fig. 2g) and observed clusters with heavy neutrophil infiltration (and some macrophages) or tumors enriched with macrophages of various subtypes.

Taken together, using different approaches and patient cohorts, we observed heterogeneous tumor immune microenvironments characterized by the divergent infiltration of neutrophils and macrophages.

Tumor-intrinsic factors contribute to myeloid cell profiles

The variations of TIN/TIM frequency within each model are much smaller compared to overall variations across all models (Fig. 3a), suggesting that TIN/TIM frequency is a relatively stable trait. Some other immune cells are also enriched or depleted in specific models (Supplementary Fig. 3a), but exhibited less variation and lower overall frequencies (Supplementary Table 1).

We co-transplanted T11 (MES) and 2208L (NES) tumors into contralateral mammary glands of the same animals (Fig. 3b). This did not alter TIN/TIM frequency (Fig. 3b), further supporting that the TIN/TIM frequency is in part determined by tumor-intrinsic factors. Interestingly, T11 tumors displayed minimal neutrophil infiltration even in presence of systemic neutrophil accumulation (induced by the contralateral 2208L tumors) (Supplementary Fig. 3b), suggesting an active neutrophil-repelling mechanism.

MMTV-PyMT is an exception: 28 spontaneous tumors derived from 6 animals exhibited diverse TIN/TIM frequency (Fig. 3c). We chose one tumor with intermediate levels of TIN and TIM, and performed animal-to-animal transplantation of small tumor fragments (one per animal). This operation resulted in two primary tumor lines with stable TIN/TIM frequency, named PyMT-M ("macrophage-enriched") and PyMT-N ("neutrophil-enriched") (Fig. 3c

and Supplementary Fig. 3c). Like other NES tumors, PyMT-N induced systemic neutrophil accumulation (Supplementary Fig. 3d). Thus, the original MMTV-PyMT tumor harbored separate TIM- and TIN-enriched regions, which may be explained by the polyclonality of PyMT tumors[48]. Importantly, the TIM/TIN frequencies of transplanted tumors are within the spectrum of spontaneous tumors, suggesting that the MES/NES phenotypes are unlikely a result of transplantation-induced inflammation (Fig. 3c). We also compared spontaneous and transplanted MMTV-WNT1 tumors, and observed no significant differences in TIM/TIN frequencies (Supplementary Fig. 3e).

The frequency of TIN is determined by tumor-derived chemo-attractants

Is the TIN/TIM dichotomy *in vivo* is recapitulated by *in vitro* chemotaxis of neutrophils or monocytes? To answer this question, we assessed chemo-attraction of bone marrow neutrophils and monocytes by tumor conditioned medium (CM) of the eight models. The variations in chemotaxis (Fig. 3d, e) can be partially explained by expression of chemokines/cytokines known to attract these cells as assessed by RNA-seq (Fig. 3d, f) or qPCR (Supplementary Fig. 3f). In particular, *Tnfaip6* encodes TSG6, which binds CXCL1/2 and inhibits neutrophil migration[49]. It is expressed in 3/4 MES models, and may mediate neutrophil repulsion[49] (Fig. 3b).

Neutrophil migration *in vitro* tightly correlated with TIN frequency *in vivo* (Fig. 3g), suggesting that tumor cell-derived chemokine/cytokines contribute to TIN accumulation. In contrast, monocyte migration only weakly correlated with monocyte frequencies *in vivo* (Fig. 3h), and did not correlate with TIM frequencies (Supplementary Fig. 3h).

Alteration of epithelial-mesenchymal transition (EMT) tilts TIN/TIM balance

When cultured *in vitro*, the eight tumor models exhibited different cell morphologies. Three NES models, 2208L, 4T1, and PyMT-N, were cobblestone/epithelial-like, whereas all MES models were spindle/mesenchymal-like. AT3 was unique: single cells scatter but are not spindle-like (Fig. 4a). Transcriptomic profiling largely confirmed the epithelial and mesenchymal properties, and classified AT3 as mesenchymal (Fig. 4b). Expression of key genes, *Zeb1* and *Cdh1*, was validated by qPCR (Supplementary Fig. 4a). Thus, EMT is associated with the TIN/TIM frequency and NES/MES subtyping.

Zeb1 was up-regulated in all mesenchymal lines (Fig. 4b). The reciprocal inhibition between miR-200 family and Zeb1 regulates EMT[50–53]. miR-200c expression is higher in epithelial NES tumors (Supplementary Fig. 4b). miR-200c overexpression in MES reduced *Zeb1* (Fig. 4c), shifted cells towards an epithelial phenotype as assessed by an EMT reporter and cell morphology (Supplementary Fig. 4c, d), increased neutrophil-recruiting chemokines including *Cxcl1*, and decreased the neutrophil-repelling molecule *Tnfaip6* (Fig. 4c). Short hairpin RNA-mediated *Zeb1* knockdown elicited similar changes (Supplementary Fig. 4e). miR-200c expression in human MDA-MB-231 cells also reduced *TNFAIP6* and increased the functional *Cxcl2* homolog, *IL8* (Fig. 4c). Consistently, miR-200c overexpression promoted *in vitro* neutrophil migration in trans-well assays (Fig. 4d), but slightly (statistically significant in one of four models examined) decreased monocyte-related chemo-/cytokine CCL2 and M-CSF (Supplementary Fig. 4f) and corresponding *in vitro*

monocyte migration (Supplementary Fig. 4g). Finally, miR-200c expression in T11 tumors *in vivo* caused a TIN increase but a TIM decrease (Fig. 4e). Thus, perturbation of EMT reprograms tumor myeloid microenvironment.

In the TCGA dataset, we used GSEA to identify pathways correlative with TIMER-derived TIM and TIN scores (Fig. 4f). EMT is the top pathway specifically associated with TIM (Supplementary Fig. 4h), supporting our observations in mouse models. The TIN-associated pathways include PI3K-AKT-mTOR (Supplementary Fig. 4i), consistent with previous findings that the mTOR signaling causes gMDSCs accumulation[33]. Gene Set Variation Analysis (GSVA)[54] reinforced the connection between EMT/mTOR pathways and TIM/TIN. Two different EMT signatures[55,56] are associated with monocyte/macrophage-recruiting cytokines *CSF1* and *CCL2*, neutrophil-repelling molecule *TS6G* (Fig. 4g), and TIM scores (Supplementary Fig. 4j). PI3K/AKT/mTOR pathway is associated with neutrophil-recruiting chemokines *CXCL1* and *IL8*, and TIN scores (Fig. 4g). Finally, miR-200c expression inversely correlated with TIM scores (Fig. 4h). Thus, tumor-intrinsic pathways contribute to the development of diverse myeloid cell compartment. In particular, EMT may simultaneously drive monocyte/macrophage recruitment and neutrophil exclusion.

TIMs in MES and NES exhibit different CCR2-dependency and interactions with TINs

We profiled TIM transcriptomes in four models representative of different genetic background and immune subtypes. Principle component analysis suggested multi-polar TIM polarization (Fig. 5a). GSVA indicated that T11-TIMs overexpress multiple immunosuppressive Hallmark Pathways including TGFβ, reactive oxygen species (ROS), and mTOR[57,58], whereas E0771-TIMs overexpress pro-inflammatory pathways including IFNγ and TNFα (Fig. 5b and Supplementary Fig. 5a). Similar to T11-TIMs, AT3-TIMs overexpress several immunosuppressive pathways like Myc and ROS, but also highly express pro-inflammatory pathways like TNFα.

The functional impact of TIMs was evaluated by transplantation of various tumors into *CCR2* knockout (CCR2-KO) mice. As expected, Ly6C^{high} monocytes were reduced by 3- to 7-fold in all models (Fig. 5c). However, a significant TIM reduction (fold change > 2 and $p < 0.05$) was only seen in MES tumors (Fig. 5c), indicating MES-specific CCR2-dependency. In contrast, NES-TIMs were not affected by CCR2-KO.

The impact of CCR2-KO was heterogeneous on tumor growth (Supplementary Fig 5b), T cell infiltration (Supplementary Fig. 5c), proliferation, apoptosis or angiogenesis (Supplementary Fig. 5d). Nevertheless, the inverse relationship between TIMs and TINs was evident, i.e., whenever TIMs were reduced, TINs increased (Fig. 5c–e). This effect was systemic in MES tumor-bearing animals (Supplementary Fig. 5e), but did not occur in tumor-free animals (Supplementary Fig. 5f). Because in two NES models CCR2-KO failed to reduce TIMs, we used combined CSF1-neutralizing antibody (anti-CSF1) and clodrosome to deplete TIMs. This approach can eliminate tissue-resident macrophages, and indeed depleted TIMs in all models tested including NES (Fig. 5f). Interestingly, whereas anti-CSF1+clodrosome treatment in MES resulted in increased TINs, confirming the CCR2-KO

results, it failed to induce a similar increase in NES (Fig. 5f). Thus, the negative impact on TINs appears specific to CCR2-dependent TIMs.

Neutrophils in NES are immunosuppressive

TIN transcriptomes of E0771, T11, 2208L, and AT3 tumors were also profiled. We used previously identified gene signatures to distinguish normal neutrophils from gMDSCs and/or tumor-associated neutrophils (TANs)[59]. NES-TINs (2208L and AT3) express a substantial proportion of TAN/MDSC genes, whereas MES-TINs (T11 and E0771) are more related to normal neutrophils (Fig. 6a). GSVA of the Hallmark Pathways further uncovered differences of TINs between NES and MES. The former displayed enhanced expression of several immunosuppressive pathways, including STAT3, TGFβ and ROS (Fig. 6b and Supplementary Fig. 6a)[60,61]. In addition, the NOTCH pathway is elevated – supporting a previously reported feedback loop between MDSCs and tumor-initiating cells (Fig. 6b)[33]. A search in additional gene sets revealed adenosine metabolism (Supplementary Fig. 6b) as another immunosuppressive pathway[62,63] up-regulated in NES-TINs. $CD11b^{+}Ly6G^{+}$ cells in the bone marrow of NES tumor-bearing animals suppressed T cell proliferation *in vitro* (Fig. 6c), thereby meeting the definition of gMDSCs [37,64]. Thus, TINs in different immune subtypes differ in both frequencies and immunosuppressive activities. Moreover, NES tumors induce systemic accumulation of gMDSCs.

Given the negative impact of TIMs on TINs recruitment in MES, we asked if a reciprocal regulation occurs in NES. By applying anti-CXCR2+ anti-Ly6G, we reduced NES-TINs by 2- to 10-fold. This resulted in an increase of Ly6C+ monocytes but not TIMs (Fig. 6d, e), suggesting a negative regulation of TIN on monocyte recruitment. The increased monocytes did not differentiate into TIMs. In contrast, monocytes in MES readily differentiate into TIMs (Fig. 5c). Thus, the definition of MES includes tumors enriched with TIMs and their precursor monocytes.

NES and MES respond differently to immune checkpoint blockade (ICB)

We subjected eight models (4 NES, 3 MES, and MMTV-WNT1 as a representative “cold” tumor) to ICB therapy (anti-PD1+anti-CTLA4). The NES and cold tumor never responded (Fig. 7a) even when the dosage was escalated to the maximum tolerable level (Supplementary Fig. 7a). MES showed largely variable responses (Fig. 7a and Supplementary Fig. 7a). We also observed that MES tumor-derived cell lines (e.g., PyMT-M), when transplanted, gave rise to tumors exhibiting stronger ICB responses than tumors derived from tissue fragments of the same model (Fig. 7a vs. Supplementary Fig. 7b). However, NES-derived cell line (e.g. PyMT-N) remained resistant (Supplementary Fig. 7b). TINs may create an immunosuppressive microenvironment independent of checkpoints, rendering these tumors non-responsive to ICB. ICB responses do not correlate with baseline tumor-infiltrating $CD8^{+}$ T cells (Supplementary Fig. 7c) or PDL1 expression (Supplementary Fig. 7d). However, MES, but not NES, exhibited increased $CD8^{+}$ T cell infiltration post-treatment, and sometimes a reduction of % PD1+ T cells (Supplementary Fig. 7e), suggesting that ICB restores CD8+ T cell activity in MES.

Although MES exhibited better responses than NES, the extent varied. T11 is enriched with immunosuppressive TIMs (Fig. 5b), and CCR2 KO improved ICB responses: 5/5 T11 tumors regressed completely (Fig. 7b). The same treatment in E0771 and PyMT-M did not significantly alter responses (Supplementary Fig. 7f).

We asked if immunosuppressive TINs mediate *de novo* ICB resistance. TIN reduction by combined anti-CXCR2 and anti-Ly6G treatment did not lead to improved ICB responses in NES (Supplementary Fig. 7g), perhaps due to the compensatory increase of immunosuppressive monocytes (Fig. 6d), as indicated by T cell proliferation assay (Supplementary Fig. 7h). ICB resistance was confirmed by lack of alterations in T cell frequencies or $PD1^+$ proportion (Supplementary Fig. 7i).

MES accumulates immunosuppressive TINs when acquiring resistance to ICB

E0771 tumors (>90%) exhibited durable responses to ICB, even after treatment cessation. One tumor recurred with increased TINs, which was designated E0771-ICBR. When further transplanted, neutrophil accumulation persisted both locally and systemically (Fig. 8a). Moreover, E0771-ICBR expresses increased *Cxcl1* and reduced *Tnfaip6* (Fig. 8b). Neutrophils from E0771-ICBR-bearing animals potently suppressed T cell proliferation, displaying features of gMDSC (Fig. 8c), and were $Ly6G^{low}$ (Supplementary Fig. 8a), representing immature neutrophils[39,65]. The recurrent tumors accumulated neutrophils in the bone marrow (Supplementary Fig. 8b, c) and led to splenomegaly (Supplementary Fig. 8d). These alterations mirrored NES, and suggest MES-to-NES switch upon acquisition of ICB resistance. Combination of anti-Ly6G and ICB reduced recurrence by 50% and significantly improved progression-free survival of the tumor-bearing animals (Fig. 8d, e).

Similar results were obtained in PyMT-M. Cell line-derived PyMT-M tumors exhibited tumor stasis or regression upon ICB (Supplementary Fig. 7b). A recurrent derivative (PyMT-M-ICBR) showed significantly increased accumulation of TINs locally and systemically (Supplementary Fig. 8e). *Cxcl1/2* expression was increased, whereas *Tnfaip6* was decreased (Supplementary Fig. 8f).

Thus, accumulation of immunosuppressive TINs or gMDSCs is associated with acquired ICB resistance in MES, and targeting these cells may alleviate resistance to ICB.

Exceptional neutrophil accumulation is associated with poor patient outcome

We used published metastatic melanoma datasets to query TIN roles in ICB response in human tumors, since relevant datasets are not yet available for TNBC. TIMER was applied to predict immune cell infiltration (Fig. 8f, h). In one dataset (Fig. 8f)[66], TIN scores were significantly higher in patients with progressive disease (PD) or partial response (SD/PR), than those exhibiting a complete response (CR) (Fig. 8g). In another dataset[67], 70% of patients with PD were either top- or bottom-ranked according to the TIN score (Fig. 8h). We observed a significant inverse correlation between TIM and TIN scores ($R=-0.53$, $P=0.0033$). Low-TIN tumors might enrich TIMs that attenuate ICB efficacy, similar to T11 (Fig. 7b). Normality tests revealed 20% of tumors beyond a normal distribution, representing a distinct TIN-enriched group (Supplementary Fig. 8g, h). Applying the 20% cutoff and combining both datasets, we found a PR depletion and PD enrichment in NES-like

melanoma (Supplementary Fig. 8i), supporting the correlation between heightened neutrophil accumulation and ICB resistance.

DISCUSSION

One possible limitation of our study is the usage of transplantable tumors (cell lines or primary tissues). Tissue injury during transplantation and the absence of natural tumorigenesis may influence immune cell profiles. In two models, we compared spontaneous tumors with their transplantable derivatives, and found no significant difference in TIM/TIN frequency (Fig. 3c and Supplementary Fig. 3e). Genetically engineered models with spontaneous tumors also have caveats. Thus, it is important to compare the immune landscape of pre-clinical models to human tumors, and ideally at a single-cell level.

Different immune subtypes may co-exist intra-tumorally as demonstrated in PyMT. NES and MES tumors can be co-transplanted to a single host without affecting one another. This mutual exclusivity may result from the strong attraction of neutrophils in NES, whereas MES appears to repel neutrophils through EMT-mediated inhibition of neutrophil chemotaxis. Furthermore, neutrophils and monocytes/macrophages appear to negatively regulate each other, consistent with a previous report[68]. These mechanisms may cause spatial segregation between MES and NES within a same tumor.

Our data suggest different TIM biology between MES and NES tumors. In MES, TIMs are derived from CCR2+ monocytes, may be polarized to M1-like or M2-like, and negatively regulate TIN recruitment. In NES, TIMs are not clearly M1-M2 polarized, impacted by CCR2 KO, or regulating TINs. These observations suggest more complicated biology of NES-TIMs, perhaps involving different cell-of-origin, differentiation, proliferation or activation.

NES tumors drive systemic gMDSC accumulation. However, MES-TINs are more similar to normal neutrophils, and might even perform anti-tumorigenic functions as previously shown[9]. Thus, the functions of TINs are determined by the entire myeloid compartment, further highlighting the importance of investigating the interaction among multiple cell types.

Previous studies linked EMT to immunosuppression as EMT up-regulates checkpoint molecules in cancer cells[69,70]. Here, we show that reversion of EMT may be accompanied by an influx of neutrophils, thereby switching the source of immunosuppression to neutrophils.

A recent study suggested that loss of p53 dictates systemic accumulation of pro-metastasis neutrophils in breast cancer (71). One of our models (T11) lacks p53 but did not induce neutrophil accumulation, suggesting more complicated mechanisms. The present and a previous study from our laboratories (33) indicate that additional tumor-intrinsic pathways (e.g., EMT and mTOR) and interplay between different immune cell populations (e.g., neutrophils and macrophages) need to be considered.

Overall, our studies highlight systematical characterization of microenvironmental heterogeneity – by integrating multiple cell types in multiple tumor models, and that the heterogeneity of breast cancer extends to the immune microenvironment. Therefore, in addition to mutation load and antigenicity, the tumor myeloid compartment need to be examined to tailor immunotherapies.

METHODS

Mice

All animal experiments were conducted in accordance with a protocol approved by Institutional Animal Care and Use Committee of Baylor College of Medicine. The study is compliant with all relevant ethical regulations regarding animal research.

Female animals of 6 – 8 weeks are used as the recipients of tumor tissue or cell line transplantation. Age-matched mice (10 – 12 weeks) were subjected to euthanization for immune profiling in all experiments. BALB/cAnNHsd (BALB/c), C57BL/6NHsd (C57BL/6 or B6), FVB, C.B-17/IcrHsd-*Prkdc*^{scid}*Lyst*$^{bg-J}$ (SCID-beige) were purchased from Envigo and either directly used for experiments or bred in our facilities. B6.129S4-*Ccr2*^{tm1Ifc}/J (CCR2 KO), B6.FVB-Tg(MMTV-PyVT)634Mul/LellJ (MMTV-PyMT), B6.Cg-*Foxp3*^{tm2Tch}/J (B6. FOXP3-GFP), C.Cg-*Foxp3*^{tm2Tch}/J (BALB/c. FOXP3-GFP), and C57BL/6J (wild-type) were purchased from The Jackson Laboratory and bred in our facilities. To generate CCR2 KO mice in BALB/c background, CCR2 KO mice were crossed with wild-type BALB/c mice for five generation.

Breast tumor models and transplantation

Primary tumor tissue lines were maintained by implanting 1 – 2 mm^3 size tumor pieces and cryopreserving as chunks upon tumor harvest. Tumor models include T11 (BALB/c, p53-null tumor), 2208L (BALB/c, p53-null tumor), T1 (BALB/c, p53-null tumor), T12 (BALB/c, p53-null tumor), 2151R (BALB/c, p53-null tumor), 2245R (BALB/c, p53-null tumor), PyMT-M and -N (B6, MMTV-PyMT sub-lines), MMTV-WNT1 (FVB), P53-PTEN DKO (FVB). The P53-PTEN DKO tumor tissue used for transplantation was derived from MMTV-cre;Trp53F/F;PtenF/F strain which was directly bred by Dr. Jianming Xu's lab at Baylor College of Medicine.

Cell lines were derived from above models and maintained as described in Cell lines and cell culture section. For inoculation into animals, cells were collected from culture with 0.25% trypsin (HyClone), washed with PBS (Lonza), counted, re-suspended in 1:1 solution of PBS and Matrigel (Pheno Red-free and growth factor reduced; BD Biosciences), and injected into 4th mammary fat pad. Tumor models include 4T1 (BALB/c, 0.5 X 10^6 cells), 4T07 (BALB/c, 1 X 10^6 cells), 67NR (BALB/c, 1 X 10^6 cells), T11 (BALB/c, 0.5 X 10^6 cells), AT3 (B6, 0.5 X 10^6 cells), E0771 (B6, 0.5 X 10^6 cells), E0771-ICBR (B6, 0.5 X or 1 X 10^6 cells), PyMT-M and -N (B6, 0.5 X 10^6 cells), PyMT-M-ICBR (B6, 0.5 X 10^6 cells). Genetic background and cell number used for transplantation are indicated in parenthesis.

PDXs were maintained by implanting 1 – 2 mm^3 size tumor pieces into fat-pad cleared mammary glands of SCID-Beige mice. The development of PDX lines was conducted under

the Institutional Review Board-approved protocols. The current study used already-established PDXs that had been de-identified, and therefore, has been granted protocol exemption by the Institutional Review Board for not involving human subjects.

Mammary fat pad transplantation/injection was performed using the same procedures as our previous studies[33,34].

Cell lines and cell culture

All cell lines were cultured in DMEM/High Glucose medium (HyClone) except for E0771 (both parental and ICBR). E0771 (CH3 Biosystems) was cultured in RPMI-1640 medium (HyClone, supplemented with 10mmol/L HEPES (Gibco)). All media contained 10% FBS, 100U/ml penicillin, 100 ug/ml streptomycin (Lonza), and 250ng/ml amphotericin B (Lonza), except that for 67NR which was further supplemented with NEAA (Life technologies, cat # 11140050). All cells were grown in a humidified incubator at 37°C, with 5 % CO_2. More information about cell lines can be found in "Eukaryotic cell line" section of Reporting Summary.

Human TNBC tissues

The TNBC nanostring dataset (n=72) was collected under institutional review board-approved protocol at Scott and White Medical Center, Baylor Scott and White Healthcare. Informed consent from all participants were obtained. The other human datasets are all deidentified, and obtained from publicly available sources (e.g., TCGA), which were collected under institutional review board–approved protocols at the original authors' institutions. The study is compliant with all relevant ethical regulations regarding research involving human participants. Raw macrophage counts (CD68 positive) for IHC staining (Fig. 2b and 2c) are provided in the rightmost column in Supplementary Table 2c. In Fig. 2d, a continuous score of each tumor was computed by $\Sigma \log_2(\text{MSGi})$ in which MSGi represents individual macrophage-specific gene. These scores were compared against quantitative IHC scores of CD68. Since a large proportion of specimens on TMA were scored 0 and the rest data were sparsely distributed across a large range, we treated IHC scores as a categorical variable and use 10 as a cutoff to define two groups: negative/weak (< 10) or strong (>10).

miR-200c induction *in vitro* and *in vivo*

T11, PyMT-M, E0771 and MDA-MB-231 were transduced with doxycycline inducible miR200c over-expression vector pINDUCER13-pre-miR-200c/141 (p13-miR-200/141) and selected for at least 3 days in 2 μg/mL puromycin. T11 and MDA-MB-231 cell lines were also transduced with Z-Cad sensor[53] that can identify carcinoma cells with EMT or MET properties, respectively. To induce miR-200c/141 *in vitro*, cells were treated with doxycycline (DOX) (sigma) for 1 – 2 weeks: 2 μg/mL for T11 and PyMT-M, 500 ng/mL for E0771, and 100 ng/mL for MDA-MD-231. To induce miR-200c/141 in T11 *in vivo*, cells were first treated with 2 μg/mL DOX for 2 weeks *in vitro* prior to inoculation to mice. DOX was administered to animals from Day 1 post-tumor implantation till tumor harvest (2 weeks). Harvested tumors were immune profiled as well as re-transplanted to another batch of mice for further DOX induction (another 2 weeks) and immune profiling. Data were

combined and analyzed from both batches. DOX solution of 1 mg/ml was freshly prepared once a week, using 5% sucrose in water as the vehicle.

Lentivirus transduction of tumor cells

T11 cells were transduced with mouse ZEB1-specific shRNA (5'-ATATGTGAGCTATAGGAGC −3') or a scramble-control non-specific shRNA using the lentiviral pGIPZ vector system that allows puromycin selection to obtain pure transduced cell population.

In vivo drug treatment for immune checkpoint blockade (ICB) and combination therapy

On Day 0 of experiments, tumor tissue pieces or cell lines were implanted orthotopically as specified in the previous session. Animals were randomized when tumors reached similar size (4 – 5 mm in diameter) and given treatments with the following regimen for each drug. To size match tumors, MMTV-Wnt1 tumor-bearing animals received initial treatment at various time points following transplantation due to variable tumor latency. 67NR was not included for this analysis due to its distinct growth kinetics, which makes it difficult to compare to all other models with regards to therapeutic response.

In Fig. 7a, 100 μg anti-CTLA4 (clone 9D9) and 200 μg anti-PD1 (clone RMP1–14) antibody were delivered every three days until end point (total 4 – 6 doses). In Supplementary Fig. 7a, treatment was initiated Day 1 post-tumor implantation and continued every other day till end-point.

In Fig. 7b and Supplementary Fig. 7b and 7f, on Day 0 of experiment, 0.5 X 10^6 cells of T11-derived cell line, E0771, PyMT-M and -N-derived cell lines were inoculated orthotopically and randomized on Day 5 for treatment initiation. ICB treatment was given every three days with the same dosage as described above (total 8 doses for T11, total 4 doses for E0771 and PyMT-M and -N).

In Fig. 8d, for first 4 doses animals were given 100 μg anti-Ly6G (clone 1A8) every three days together with ICB (same dosage as described above), and for next 8 doses given 200 ug anti-Ly6G without ICB every three days.

In Fig. 6d and Supplementary Fig. 7g, 100 ug (5 mg/kg) of anti-Ly6G (clone 1A8) and 200 ug (10 mg/kg) of CXCR2 inhibitor (Selleckchem, SB225002) were administered i.p. every three days from tumor palpation until end point. ICB treatment was given every three days with the same dosage as described above. SB225002 was dissolved in DMSO and with 30 % PEG300 (Sigma), 5 % Tween 80 (Sigma) in D.W.

In Fig. 5f, 0.5 mg of anti-CSF1 (clone 5A1) and 100 ul of clodrosome (Encapsula Nanosciences) were delivered through i.p. and i.v. (retro-orbital) injection respectively and administered every five days, two-to-three days spaced between different treatments. Treatment was initiated day 2 post-tumor transplantation for T11, PyMT-N, 2208L, and upon tumor palpation for PyMT-M, and continued until end point (total 3– 6 doses).

Control animals received an equal amount of isotype-matched antibodies (mouse IgG2b (clone MPC-11), rat IgG2a (clone 2A3), and rat IgG1 (clone HRPN)). All antibodies were delivered intraperitoneally and were purchased from BioXcell. Tumors were measured with a caliper and the volume was calculated using the formula $\pi/6$ x Width^2 x length.

Spontaneous pulmonary metastasis assay

Assay was performed using eight tumor models implanted as either tissues or cell lines (10^5 – 2×10^5 cells in 100 μl PBS) by orthotopic transplantation to mammary fat pads, followed by tumor resection when tumors reached ~ 1 cm^3. The mice were closely monitored for one of the following endpoints: 1) recurrent tumors reach 2 cm^3; 2) significant signs of morbidity; or 3) 4 months after resection. Lungs were extracted for examination of macroscopic metastases as previously described[34].

Tissue harvest and dissociation

Tumor was resected when it reached approximately the size of 1 gram. For RNA-seq and immune cell profiling, orthotopic breast tumors were collected in ice-cold PBS and subjected to dissociation using Tumor Dissociation Kit, mouse (Miltenyi Biotec) following supplier's protocol. Tumors (0.2 – 0.4 g) were cut into small pieces (around 1mm^3) and transferred to gentleMACS C tubes (Miltenyi) containing 2.35 ml of RPMI 1640, 100 μl of enzyme D, 50 μl of enzyme R, and 25 μl of enzyme A. Tissues were mechanically dissociated on a gentle MACS Dissociator (Miltenyi). Three consecutive 'm_Lung_02' program was briefly run on the dissociator, spaced with 10 min shaking incubation at 37°C in between. The dissociation reaction was stopped with ice-cold RPMI-1640 and a single cell suspension was obtained by filtering through 70-μm cell strainer (Greiner Bio-One). The single cell suspension was centrifuged for 5 min at 350g, re-suspended in 1 ml RBC lysis buffer (eBioscience), incubated on ice for 1 min, and washed with 10 ml FACS buffer (PBS containing 1% FBS). Samples with >90% cell viability were used for further analyses.

Blood was drawn and collected in 0.5 M EDTA-coated tubes. To separate plasma from blood cells, a 15 min centrifugation at 1,500g, 4°C was performed. Whole bone marrow and splenic immune cells were isolated by crushing the respective organ, and single cell suspension was obtained by filtering through 70-μm cell strainer. Erythrocytes were lysed with RBC lysis buffer (Tonbo, cat # TMB-4300-L100) by incubating on ice for 10 min, after which cells were washed with FACS buffer.

Flow cytometry

Single cell suspension was prepared as described in Tissue harvest and dissociation section. Cells were incubated for 10 min on ice with FcR blocker (1:100, clone 2.4G2, Tonbo) in FACS buffer. Cells were subsequently stained with directly conjugated antibodies in FACS buffer for 25 min on ice in the dark, followed by two washes with FACS buffer. FOXP3+ regulatory T cells were identified by endogenous GFP signal from reporter mice (B6. FOXP3-GFP, BALB/c FOXP3-GFP). Stained cells were immediately analyzed or fixed with 0.5% PFA in PBS. All data were acquired using BD LSR Fortessa or LSRII Analyzer, and analyzed with Flow Jo v10.0. The absolute number of tumor-infiltrating immune cells (over total number of cells in single cell suspension) was determined by using the liquid counting

beads (BD Biosciences). The following antibodies were used for FACS sorting as well as immune profiling.

Myeloid cell phenotyping panel I: CD45-violetFluor450 (clone 30-F11, Tonbo), CD11b-APC-Cy7 (clone M1/70, Tonbo), Ly6G-PerCPcy5.5 (clone 1A8, Tonbo), Ly6C-PE-CF594 (clone AL-21, BD Biosciences), F4/80-BV605 (clone BM8, Biolegend), I-A/I-E-BV510 (clone M5/114.15.2, Biolegend), CD11c-AlexaFluor700 (clone N418, Biolegend), CD64-APC (clone X54–5/7.1, Biolegend), CD103-PE-Cy7 (clone 2E7, Biolegend), PDL1-BV711 (clone MIH5, BD Biosciences), DAPI (NucBlue Fixed Cell ReadyProbes Reagent)

Myeloid cell phenotyping panel II: CD45-violetFluor450 (clone 30-F11, Tonbo), CD11b-APC (clone M1/70, Tonbo), Ly6G-PerCPcy5.5 (clone 1A8, Tonbo), Ly6C-BV711 (clone HK1.4, Biolegend), F4/80-FITC (clone BM8, eBioscience), I-A/I-E-BV510 (clone M5/114.15.2, Biolegend), CCR2-PE (R&D systems)

Lymphoid cell phenotyping panel I: CD45-violetFluor450 (clone 30-F11, Tonbo), B220-APC-Cy7 (clone RA3–6B2, Biolegend), CD3e-PerCPcy5.5 (clone 145–2C11, Tonbo), CD4-APC (clone GK1.5, Tonbo), CD8-FITC (clone 53–6.7, Tonbo), CD25-BV510 (clone PC61, BD Biosciences), PD1-BV605 (clone 29F.1A12, Biolegend), γδTCR-PE (clone GL3, Biolegend), DAPI (NucBlue Fixed Cell ReadyProbes Reagent)

Cell sorting and library preparation for RNA-seq

To obtain pure tumor-infiltrating neutrophils (TINs) and macrophages (TIMs), breast tumors were dissociated into single cell suspension by the same method as described in Tissue harvest and dissociation section. FACS sorting was performed using Aria Cell Sorter (BD Biosciences) to purify TINs (DAPI- CD45+ CD11b+ Ly6G+ Ly6C med-low) and TIMs (DAPI- CD45+ CD11b+ Ly6G- Ly6C- F4/80+). Cells were directly sorted into TRIzol LS (Invitrogen), and kept at −80°C until further processing. RNA was extracted using the Direct-Zol RNA microprep kit (Zymo Research).

Following RNA isolation, MATQ-seq was performed to amplify the whole transcriptome TINs and TIMs as previously described[34]. Regular RNA-seq was performed for cancer cells' RNA. The pair-ended reads were mapped to the mouse genome (UCSC mm10) using STAR (https://github.com/alexdobin/STAR) with NCBI RefSeq genes as the reference.

RNA isolation and quantitative real-time polymerase chain reaction

We followed procedures described in our previous publication for RNA isolation and qPCR[34]. The primers are listed in Supplementary Table 4.

In vitro trans-well migration assay

Bone marrow immune cells were harvested immediately from euthanized 8 week old naïve wild-type (BALB/c and B6) mice as described above (Tissue harvest and dissociation section). Following RBC lysis, neutrophils were enriched by positive selection using biotinylated anti-mouse Ly6G (clone 1A8, Biolegend) and Ly6C high monocytes were enriched by negative selection using biotinylated anti-mouse antibodies against B220, CD3e (BD Pharmingen, cat # 559971), and Ly6G (clone 1A8, Biolegend) as per protocol of

EasySep Mouse Biotin Positive Selection Kit (STEMCELL techonlogies). For trans-well migration assay, tumor-conditioned medium (TCM) containing 0.2 % FBS (cultured 24 hours) was added to the bottom of 24 well plate. 1 X 10^6 cells of either neutrophils or monocytes (in the same medium used to generate TCM) were added to upper chamber trans-well inserts: 3 μm pore size for neutrophils (Corning, cat # 3415) and 8 μm pore size for monocytes (Corning, cat # 3422). Cells were incubated at 37°C for 2 hours (neutrophils) or 4 hours (monocytes), following which inserts were removed, and cells in bottom well were harvested. Flow cytometry was used to quantify migrated cells using liquid counting beads as a reference (BD Biosciences).

In vitro T cell proliferation (suppression) assay: co-culture with neutrophils and monocytes

CD3+ T cells of naïve BALB/c or C57BL/6 mice (6 – 8 weeks old) were enriched from spleen by negative selection using biotinylated anti-mouse antibodies against B220, CD11b, Gr1 (BD Pharmingen, cat # 559971) and CD11c (BD Pharmingen, cat # 553800) followed by magnetic separation using EasySep Mouse Biotin Positive Selection Kit (STEMCELL Technologies). Bone marrow neutrophils and monocytes from either naïve or relevant tumor-bearing animals were harvested as previously described in "*In vitro* trans-well migration assay". Magnetically sorted CD3+ T cells were labeled with CFSE (5 μM, Molecular Probes) as per manufacturer's instruction. T cells were cultured alone or admixed with neutrophils or monocytes (at 1:3 ratio) in 96 well plate. T cell activation was with anti-CD3e (eBioscience, cat # 16–0031-85) through coating of wells at 5 μg/mL, overnight, 4°C and IL-2 (R&D, cat # 202-IL-010/CF) at 5 ng/mL. After 4 days of co-culture, cells were collected and analyzed for CFSE intensity by flow cytometry. Collected cells were also stained for Gr1-PE (ebioscience, cat # 12–5931-82) to be able to exclude non-T cells from the analysis. Proliferation index (%) was calculated as follows: (percentage of proliferated, co-cultured CD3+ T cells)/(percentage of proliferated CD3+ T cells cultured alone) X 100.

Immunofluorescence and immunohistochemistry staining

Tumor samples were fixed one day (4°C) with 10% neutral buffered formalin in PBS, incubated one day (4°C) in 30 % sucrose, and subsequently frozen in optimal cutting temperature compound. Frozen sections were permeabilized with 0.25 % Triton X-100 for 10 min at RT. After blocking for 1 hour at RT in blocking buffer (5 % goat serum, 5 % donkey serum, 2 % BSA in PBS-GT), slides were incubated overnight in a humidified chamber at 4°C with rat anti-mouse Ly6G (1:400, Tonbo, cat # 40–1276-U100) and rabbit anti-mouse CD68 (1:400, abcam, cat # 125212). Slides were incubated with Alexa Fluor 594-conjugated goat anti-rabbit and Alexa Fluor 488-conjugated donkey anti-rat secondary antibody (1:250, Jackson ImmunoResearch) for 1 hour at RT. Slides were subsequently stained with SlowFade Gold antifade reagent with DAPI (Life technologies, cat # S36936). Washing was performed in PBS between all steps. 10x, 40x images were taken with Leica DMi8 microscope with a DMC4500 camera.

Tumor samples were fixed in 10% neutral buffered formalin and paraffin-embedded. Microtome sectioning and immunohistochemistry staining was performed by the BCM Breast Center Pathology Core. Briefly, 3–4 μm thick sections were deparaffinized in xylene and graded alcohols, and treated with a heat-induced antigen retrieval buffer Tris-HCL 9.0 in

a pressure cooker. Slides were blocked in 3% hydrogen peroxide solution for 5 min at RT. Primary antibodies were incubated for 1 hour at RT in antibody diluent solution (1% BSA in TBS-20) and subsequently stained with Envision Labeled Polymer-HRP anti-rabbit (Dako) for 30 min at RT. Slides were incubated with DAB+ solution (DakoCytomation) for 15 min at RT, and with DAB Sparkle Enhancer (Biocare) to enhance the chromogen signal. Afterwards counterstaining in Harris Hematoxylin was performed and coverslip was mounted. Washing was performed in TBS-20 between all steps. Primary antibodies include: estrogen receptor (Santa Cruz, sc-542, 1:800), progesterone receptor (Dako, A0098, 1:100), ErbB2 (NeoMarkers, RB-103-P, 1:400), Cleaved Caspase 3 (Cell Signaling, 9661, 1:50), Ki67 (Cell Signaling, 122025, 1:400) and CD31 (Abcam, AB-124435, 1:400). Immunohistochemical images were obtained using an Olympus BX50F4 microscope and cellSens. All pictures are representative of at least three biological replicates in each group.

Cell morphology analysis

Cancer cell images were captured at a magnification of 10x using Leica confocal microscope. 50,000 FACS-purified neutrophils (CD45+ CD11b+ Ly6G+ Ly6C med-low) and macrophages (CD45+ CD11b+ Ly6G- Ly6C- F4/80+) were cyto-spun and dried slides were stained with Wright-Giemsa Stain (Sigma-aldrich). Images were obtained at a magnification of 40x using Leica DMLB microscope.

Bioinformatics analyses

Characterization of the eight syngeneic murine tumor models—RNA-seq was performed on the 8 cell line models in technical triplicates as shown in Supplementary Fig. 1a. Genes corresponding to different properties of these cells were used for 1) TNBC heterogeneity (Supplementary Fig. 1d), 2) cytokine expression (Fig. 3f), and EMT states (Fig. 4b). In particular, in Supplementary Fig. 1d. PyMT-N expresses GATA3, K8, and K18 and PyMT-M expresses vimentin, Zeb1, and Snail, suggesting that the two models represent luminal-like and claudin-low TBNC models, respectively.

Nanostring datasets—Formalin-fixed paraffin-embedded (FFPE) tissue was first examined with hematoxylin and eosin staining to localize invasive tumor cells and surrounding area. Roche High Pure FFPET RNA Isolation Kit was then used to purify RNAs. Macrodissection was performed, when needed. Approximately 50 ng of total RNA was used to measure the expression of 730 immune-related genes and 40 housekeeping genes using the nCounter platform (NanoString Technologies) and the PanCancer Immune Profiling Panel. Data were log base 2–transformed and normalized using housekeeping genes selected using the nSolver 2.6 package. The normalized data are provided in Supplementary Table 2c.

Derivation of Macrophage-specific and neutrophil-specific genes for analysis of TNBC nanostring data.—Over 700 gene expression profiles of a variety of human cell types were obtained from Primary Cell Atlas of BioGPS (http://biogps.org/dataset/BDS_00013/primary-cell-atlas/). All macrophage-based (regardless conditions and treatments) were grouped and subjected to two comparisons: 1) to all other cell types, and 2) specifically to all neutrophil-based transcriptomic data. Statistical Analysis of Microarray

(SAM) algorithm was employed for the comparisons and implemented by the "siggene" package of R. We used a cutoff of fold change (FC) > 16 and FDR < 0.1 were used for first comparison, and FC > 8 and FDR < 0.1 were used for the second comparison. Genes selected by both comparisons were used as MSGs. The same procedures and cutoffs were applied to identify NSG. Specific arrays used in comparisons are listed in Supplementary Table 2a. These genes were then intersected with genes contained in the nanostring TNBC dataset. 33 MSGs and 45 NSGs were identified, as listed in Supplementary Table 2b. Unsupervised hierarchical clustering was performed using the "heatmap.2" function in the "gplots" package of R. Ward clustering algorithm was used and the sample distance was defined by "Manhattan" approach (absolute distance between two vectors). The resulted cluster structures were then superimposed with the expression of CSF3, ELANE and CD68 genes, as well as IHC staining results of CD68 of the same dataset.

In Fig. 2d, ΣLog2(NSG) – Σlog2(MSG) was used to compute a single score for each tumor. The distribution of this score was examined as histogram. The bimodal distribution was approximated by the "normalmixEM" function in "mixtools" package of R.

TIMER and CIBERSORT analysis of immune cell infiltration in RNA-seq/ microarray datasets of bulk tumors—We obtained RAN-seq profiles of breast cancer from TCGA data portal in June 2016. To avoid any potential batch effects, we only chose samples profiled at UNC and stored in a folder named "RNASeqV2". 1073 profiles were collected. We then used associated IHC-determined ER/PR/Erb2 statuses to extract 112 triple negative breast cancer. We did not perform any additional selection of samples. The bar-codes or IDs of all samples included in our analyses are listed in Supplementary Table 2d.

TIMER output of TCGA tumor specimens was downloaded from the algorithm website (https://cistrome.shinyapps.io/timer/). Immune cell infiltration estimates of the corresponding 1073 TCGA breast tumors were isolated by matching the barcodes and IDs. The distribution of all six types of immune cells across TNBC and non-TNBC is displayed in Fig. 2e and Supplementary Fig. 2a by using "heatmap.2" function with the option of "Manhattan" of the distance function and the option of "Ward.D2" of the hclust function for dendrogram computation. The tSNE analyses (Fig. 2f and Supplementary Fig. 2b and 2c) were implemented by the Rtsne package of R with perplexity=10 and other parameters in default setting.

CIBERSORT output was downloaded from website provided in the reference[47]. TNBC tumors were isolated based on associated annotations and displayed by hierarchical clustering using heatmap.2 with the option of "Manhattan" of the distance function and the option of "Ward.D2" of the hclust function for dendrogram computation. The predicted relative abundance of neutrophils and macrophages were also displayed as stacked bar graphs using ggplot2 package of R in Fig. 2g.

In Fig. 4f and Supplementary Fig. 4h,i, GSEA was applied to the TCGA TNBC dataset, using TIM-TIMER scores and TIN-TIMER scores as continuous phenotypic values and Hallmark Pathway as gene sets. Pathways with $p < 0.05$ and FDR < 0.1 were selected and

displayed in Fig. 4f. The graphic output depicting correlation between TIM and EMT and between TIN and PI3K-AKT-mTOR were shown in Supplementary Fig. 4h,i, respectively.

In Fig. 4g and Supplementary Fig. 4j, we applied gene set variation analysis (GSVA) to three Hallmark pathways and an EMT signature defined by Taube et al.[55]. GSVA was implemented using gsva package of R, and under default settings except for "RNAseq=TRUE". The Taube et al signature was obtained from the supplementary tables of the original paper, and contains 91 up-regulated genes and 160 down-regulated genes. 32 genes are in common between the 91 up-regulated genes and the 200 Hallmark EMT genes. The correlation between TIMER scores and pathway GSVA scores were assessed by Pearson correlation coefficients (Supplementary Fig. 4j).

In Fig. 4i, miR-200c expression TCGA TNBC was obtained from the TCGA data portal and compared against TIM scores predicted by TIMER.

In Fig. 7f-i, we analyzed two datasets published by Riaz et al.,[66] and Hugo et al.[67]. The normalized transcriptome profiles (regularized log-transformed) were uploaded to the TIMER website to generate estimates of immune cell infiltration, which are displayed as heatmap shown in Fig. 7f and 7h with samples ordered according to the TIN scores. Z-scores of TIN were compared between different therapy response groups in the Riaz dataset (Fig. 7g). In Riaz et al., only pre-treated tumors were included.

The distribution of TIN scores was examined by histogram (Supplementary Fig. 8h), which exhibited an asymmetric pattern with long right tail. Normality tests (Shapiro test and Skew test implemented in R) confirmed this observation. We then examined the Q-Q plot and noted that approximately 20% of points fall above the normality line (Supplementary Fig. 8g). Indeed, removal of the top 20% tumors renders the rest following normal distribution (Supplementary Fig. 8h). Therefore, top 20% was determined as a cutoff to define a distinct group of tumors with exceptionally high TINs (Fig. 8i).

Bioinformatics analysis of macrophage and neutrophil transcriptomes from different tumor models.—RNA-seq data of macrophages and neutrophils were analyzed by GSVA for the 50 Hallmark gene sets (http://software.broadinstitute.org/gsea/msigdb/genesets.jsp?collection=H), using the same tools described in previous section. The results are exhibited by hierarchical clustering in Fig. 5b and 6b. Principle component analysis (PCA) was used to analyze macrophage data shown in Fig. 5a, as implemented by the "prcomp" package in R.

The pre-processed, quantile-normalized GSE43254 dataset was downloaded from GEO[59]. Genes that are differentially expressed between normal neutrophils versus gMDSCs or TANs were identified using SAM by criteria: FDR < 0.1 and fold change > 10. These genes are listed in Supplementary Table 3a, and were used to cluster the neutrophil profiles in our tumor models in an unsupervised fashion (Fig. 6a).

For GO-enrichment analyses, FDR < 0.05 were used to define TIN-enriched genes. GOstats was then carried out to calculate GO terms enriched in up-regulated and down-regulated genes in neutrophils of NES tumors. We focused on GO terms that contain more than 5

genes, P < 0.001 and odds ratio > 3. 250. Identified GO terms are listed in Supplementary Table 3b, 7 of which are related to purine metabolism or signaling. To further test the hypothesis, we downloaded 86 gene sets from MSigDB that are related to adenosine or purine by searching these keywords. GSEA was then carried out using these gene sets. 25 gene sets were scored as significant using FDR < 0.1 as a cutoff, and are listed in Supplementary Table 3c. Four representative pathways are shown in Supplementary Fig. 6b.

Statistics and Reproducibility

Data were analyzed with Microsoft Excel functions, Prism 7 software (GraphPad) or R programming language. Statistical analysis was performed using unpaired or paired two-tailed Student's *t*-test (with unequal variations if an F-test ruled out the equal variation assumption), ANOVA analysis, log-rank test (survival analysis), Fisher's exact test, Shapiro test as appropriate for the dataset. Statistical details (e.g., sample size and specific test performed) for each experiment are denoted in the corresponding figure or figure legends. Individual mouse and independent *in vitro* samples (independent batch experiments, different tumor models, different animals) were considered biological replicates. All biologically independent samples were included and combined for statistical analyses. Experimental findings were reliably reproduced. In each experiment, the group sizes were determined based on the results of preliminary experiments and no statistical method was used to predetermine sample size. Data are shown as means ± standard deviation (S.D) unless otherwise specified. In box-whisker plots, the middle line is plotted at the median, the upper and lower hinges correspond to the first and third quartiles, and the upper and lower whiskers extends no further than 1.5 * IQR from the hinges (IQR: interquartile range or distance between first and third quartiles). *P* value lower than 0.05 was considered statistically significant. The statistical source data are included in Supplementary Table 5.

Supplementary Material

Refer to Web version on PubMed Central for supplementary material.

ACKNOWLEDGEMENTS

We thank D. Weiss for critically editing the manuscript, and A. Muscarella, S. Kurley, S. Kim, J. Kim, B. Ton, L. Ma, and S.I. Abrams for providing various tumor models. X. H.-F. Z. is supported by Breast Cancer Research Foundation, NCI CA151293, US Department of Defense DAMD W81XWH-16-1-0073 and W81XWH-18-1-0574, Susan G. Komen CCR14298445, and McNair Medical Institute. J. M. R. is supported by NCI-CA16303. Flow cytometry and cell sorting was performed at the Cytometry and Cell Sorting Core at Baylor College of Medicine with funding from the NIH (P30 AI036211, P30 CA125123, and S10 RR024574) and the expert assistance of Joel M. Sederstrom.

REFERENCE

1. Joyce JA & Pollard JW Microenvironmental regulation of metastasis. Nat. Rev. Cancer 9, 239–252 (2009). [PubMed: 19279573]
2. Kim IS & Zhang XHF One microenvironment does not fit all: heterogeneity beyond cancer cells. Cancer Metastasis Rev 35, 601–629 (2016). [PubMed: 27858305]
3. Porta C et al. Macrophages in cancer and infectious diseases: the 'good' and the 'bad'. Immunotherapy 3, 1185–1202 (2011). [PubMed: 21995571]

4. Mantovani A, Sica A & Locati M Macrophage polarization comes of age. Immunity 23, 344–346 (2005). [PubMed: 16226499]
5. Schreiber RD, Old LJ & Smyth MJ Cancer Immunoediting: Integrating Immunity's Roles in Cancer Suppression and Promotion. Science (80-.) 331, 1565–1570 (2011).
6. Pyonteck SM et al. CSF-1R inhibition alters macrophage polarization and blocks glioma progression. Nat. Med 19, 1264–1272 (2013). [PubMed: 24056773]
7. Qian BZ & Pollard JW Macrophage diversity enhances tumor progression and metastasis. Cell 141, 39–51 (2010). [PubMed: 20371344]
8. Gallina G et al. Tumors induce a subset of inflammatory monocytes with immunosuppressive activity on CD8+ T cells. J. Clin. Invest 116, 2777–2790 (2006). [PubMed: 17016559]
9. Granot Z et al. Tumor entrained neutrophils inhibit seeding in the premetastatic lung. Cancer Cell 20, 300–314 (2011). [PubMed: 21907922]
10. Wculek SK & Malanchi I Neutrophils support lung colonization of metastasis-initiating breast cancer cells. Nature 528, 413–417 (2015). [PubMed: 26649828]
11. Fridlender ZG et al. Polarization of tumor-associated neutrophil phenotype by TGF-beta: 'N1' versus 'N2' TAN. Cancer Cell 16, 183–194 (2009). [PubMed: 19732719]
12. Park J et al. Cancer cells induce metastasis-supporting neutrophil extracellular DNA traps. Sci. Transl. Med 8, 361ra138–361ra138 (2016).
13. Redig AJ & Mcallister SS Breast cancer as a systemic disease: A view of metastasis. Journal of Internal Medicine 274, 113–126 (2013). [PubMed: 23844915]
14. Egeblad M, Nakasone ES & Werb Z Tumors as organs: complex tissues that interface with the entire organism. Dev. Cell 18, 884–901 (2010). [PubMed: 20627072]
15. Gabrilovich DI & Nagaraj S Myeloid-derived suppressor cells as regulators of the immune system. Nat. Rev. Immunol 9, 162–174 (2009). [PubMed: 19197294]
16. Kaplan RN et al. VEGFR1-positive haematopoietic bone marrow progenitors initiate the pre-metastatic niche. Nature 438, 820–827 (2005). [PubMed: 16341007]
17. Catena R et al. Bone marrow-derived Gr1+ cells can generate a metastasis-resistant microenvironment via induced secretion of thrombospondin-1. Cancer Discov 3, 578–589 (2013). [PubMed: 23633432]
18. Kowanetz M et al. Granulocyte-colony stimulating factor promotes lung metastasis through mobilization of Ly6G+Ly6C+ granulocytes. Proc. Natl. Acad. Sci. U. S. A 107, 21248–21255 (2010). [PubMed: 21081700]
19. Perou CM et al. Molecular portraits of human breast tumours. Nature 406, 747–752 (2000). [PubMed: 10963602]
20. Verhaak RGW et al. Integrated Genomic Analysis Identifies Clinically Relevant Subtypes of Glioblastoma Characterized by Abnormalities in PDGFRA, IDH1, EGFR, and NF1. Cancer Cell 17, 98–110 (2010). [PubMed: 20129251]
21. Lehmann BDB et al. Identification of human triple-negative breast cancer subtypes and preclinical models for selection of targeted therapies. J. Clin. Invest 121, 2750–2767 (2011). [PubMed: 21633166]
22. Carey LA et al. Race, Breast Cancer Subtypes, and Survival in the Carolina Breast Cancer Study. JAMA 295, 2492 (2006). [PubMed: 16757721]
23. Nguyen PL et al. Breast cancer subtype approximated by estrogen receptor, progesterone receptor, and HER-2 is associated with local and distant recurrence after breast-conserving therapy. J. Clin. Oncol 26, 2373–2378 (2008). [PubMed: 18413639]
24. Kennecke H et al. Metastatic behavior of breast cancer subtypes. J. Clin. Oncol 28, 3271–3277 (2010). [PubMed: 20498394]
25. Smid M et al. Subtypes of breast cancer show preferential site of relapse. Cancer Res 68, 3108–3114 (2008). [PubMed: 18451135]
26. Gentles AJ et al. The prognostic landscape of genes and infiltrating immune cells across human cancers. Nat. Med 21, 938–945 (2015). [PubMed: 26193342]
27. Li B et al. Comprehensive analyses of tumor immunity: implications for cancer immunotherapy. Genome Biol 17, 174 (2016). [PubMed: 27549193]

28. Iglesia MD et al. Prognostic B-cell signatures using mRNA-seq in patients with subtype-specific breast and ovarian cancer. Clin. Cancer Res 20, 3818–3829 (2014). [PubMed: 24916698]
29. Iglesia MD et al. Genomic analysis of immune cell infiltrates across 11 tumor types. J. Natl. Cancer Inst 108, (2016).
30. Nagalla S et al. Interactions between immunity, proliferation and molecular subtype in breast cancer prognosis. Genome Biol 14, R34 (2013). [PubMed: 23618380]
31. Maglione JE et al. Transgenic Polyoma middle-T mice model premalignant mammary disease. Cancer Res (2001).
32. Herschkowitz JI et al. Comparative oncogenomics identifies breast tumors enriched in functional tumor-initiating cells. Proc. Natl. Acad. Sci. U. S. A 109, 2778–2783 (2012). [PubMed: 21633010]
33. Welte T et al. Oncogenic mTOR signalling recruits myeloid-derived suppressor cells to promote tumour initiation. Nat. Cell Biol 18, 632–44 (2016). [PubMed: 27183469]
34. Tian L et al. Mutual regulation of tumour vessel normalization and immunostimulatory reprogramming. Nature (2017). doi:10.1038/nature21724
35. Pfefferle AD et al. Genomic profiling of murine mammary tumors identifies potential personalized drug targets for p53-deficient mammary cancers. Dis. Model. Mech 9, 749–757 (2016). [PubMed: 27149990]
36. Gautier EL et al. Gene-expression profiles and transcriptional regulatory pathways that underlie the identity and diversity of mouse tissue macrophages. Nat. Immunol 13, 1118–1128 (2012). [PubMed: 23023392]
37. Bronte V et al. Recommendations for myeloid-derived suppressor cell nomenclature and characterization standards. Nat. Commun 7, 12150 (2016). [PubMed: 27381735]
38. Coffelt SB et al. IL-17-producing gammadelta T cells and neutrophils conspire to promote breast cancer metastasis. Nature 522, 345–348 (2015). [PubMed: 25822788]
39. Casbon A-J et al. Invasive breast cancer reprograms early myeloid differentiation in the bone marrow to generate immunosuppressive neutrophils. Proc. Natl. Acad. Sci 112, E566–E575 (2015). [PubMed: 25624500]
40. Hanahan D & Coussens LM Accessories to the crime: functions of cells recruited to the tumor microenvironment. Cancer Cell 21, 309–322 (2012). [PubMed: 22439926]
41. Kusmartsev S & Gabrilovich DI Role of immature myeloid cells in mechanisms of immune evasion in cancer. Cancer Immunology, Immunotherapy 55, 237–245 (2006). [PubMed: 16047143]
42. Mabbott NA, Baillie JK, Brown H, Freeman TC & Hume DA An expression atlas of human primary cells: inference of gene function from coexpression networks. BMC Genomics 14, 632 (2013). [PubMed: 24053356]
43. Papayannopoulos V, Metzler KD, Hakkim A & Zychlinsky A Neutrophil elastase and myeloperoxidase regulate the formation of neutrophil extracellular traps. J. Cell Biol 191, 677–691 (2010). [PubMed: 20974816]
44. Semerad CL, Liu F, Gregory AD, Stumpf K & Link DC G-CSF is an essential regulator of neutrophil trafficking from the bone marrow to the blood. Immunity 17, 413–423 (2002). [PubMed: 12387736]
45. Newman AM et al. Robust enumeration of cell subsets from tissue expression profiles. Nat Meth 12, 453–457 (2015).
46. Curtis C et al. The genomic and transcriptomic architecture of 2,000 breast tumours reveals novel subgroups. Nature 486, 346–352 (2012). [PubMed: 22522925]
47. Ali HR, Chlon L, Pharoah PDP, Markowetz F & Caldas C Patterns of Immune Infiltration in Breast Cancer and Their Clinical Implications: A Gene-Expression-Based Retrospective Study. PLoS Med (2016). doi:10.1371/journal.pmed.1002194
48. Du Z et al. Introduction of oncogenes into mammary glands in vivo with an avian retroviral vector initiates and promotes carcinogenesis in mouse models. Proc. Natl. Acad. Sci. U. S. A 103, 17396–401 (2006). [PubMed: 17090666]
49. Dyer DP et al. TSG-6 Inhibits Neutrophil Migration via Direct Interaction with the Chemokine CXCL8. J. Immunol 192, 2177–2185 (2014). [PubMed: 24501198]

50. Korpal M, Lee ES, Hu G & Kang Y The miR-200 family inhibits epithelial-mesenchymal transition and cancer cell migration by direct targeting of E-cadherin transcriptional repressors ZEB1 and ZEB2. J. Biol. Chem 283, 14910–14914 (2008). [PubMed: 18411277]
51. Gregory PA et al. The miR-200 family and miR-205 regulate epithelial to mesenchymal transition by targeting ZEB1 and SIP1. Nat. Cell Biol 10, 593–601 (2008). [PubMed: 18376396]
52. Burk U et al. A reciprocal repression between ZEB1 and members of the miR-200 family promotes EMT and invasion in cancer cells. EMBO Rep 9, 582–589 (2008). [PubMed: 18483486]
53. Toneff MJ et al. The Z-cad dual fluorescent sensor detects dynamic changes between the epithelial and mesenchymal cellular states. BMC Biol (2016). doi:10.1186/s12915-016-0269-y
54. Hänzelmann S, Castelo R & Guinney J GSVA: gene set variation analysis for microarray and RNA-Seq data. BMC Bioinformatics 14, 7 (2013). [PubMed: 23323831]
55. Taube JH et al. Core epithelial-to-mesenchymal transition interactome gene-expression signature is associated with claudin-low and metaplastic breast cancer subtypes. Proc. Natl. Acad. Sci 107, 15449–15454 (2010). [PubMed: 20713713]
56. Subramanian A et al. Gene set enrichment analysis: A knowledge-based approach for interpreting genome-wide expression profiles. Proc. Natl. Acad. Sci 102, 15545–15550 (2005). [PubMed: 16199517]
57. Kaneda MM et al. PI3Kγ 3 is a molecular switch that controls immune suppression. Nature 539, 437–442 (2016). [PubMed: 27642729]
58. De Henau O et al. Overcoming resistance to checkpoint blockade therapy by targeting PI3Kγ in myeloid cells. Nature 539, 443–447 (2016). [PubMed: 27828943]
59. Fridlender ZG et al. Transcriptomic analysis comparing tumor-associated neutrophils with granulocytic myeloid-derived suppressor cells and normal neutrophils. PLoS One 7, (2012).
60. Condamine T & Gabrilovich DI Molecular mechanisms regulating myeloid-derived suppressor cell differentiation and function. Trends in Immunology 32, 19–25 (2011). [PubMed: 21067974]
61. Gabrilovich DI, Ostrand-Rosenberg S & Bronte V Coordinated regulation of myeloid cells by tumours. Nat. Rev. Immunol 12, 253–268 [PubMed: 22437938]
62. Deaglio S et al. Adenosine generation catalyzed by CD39 and CD73 expressed on regulatory T cells mediates immune suppression. J. Exp. Med 204, 1257–1265 (2007). [PubMed: 17502665]
63. Sitkovsky M & Lukashev D Regulation of immune cells by local-tissue oxygen tension: HIF1 alpha and adenosine receptors. Nat. Rev. Immunol 5, 712–721 (2005). [PubMed: 16110315]
64. Netherby CS & Abrams SI Mechanisms overseeing myeloid-derived suppressor cell production in neoplastic disease. Cancer Immunology, Immunotherapy 66, 989–996 (2017). [PubMed: 28224211]
65. Maruyama K et al. The Transcription Factor Jdp2 Controls Bone Homeostasis and Antibacterial Immunity by Regulating Osteoclast and Neutrophil Differentiation. Immunity 37, 1024–1036 (2012). [PubMed: 23200825]
66. Riaz N et al. Tumor and Microenvironment Evolution during Immunotherapy with Nivolumab. Cell 171, 934–949.e15 (2017). [PubMed: 29033130]
67. Hugo W et al. Genomic and Transcriptomic Features of Response to Anti-PD-1 Therapy in Metastatic Melanoma. Cell 165, 35–44 (2016). [PubMed: 26997480]
68. Pahler JC et al. Plasticity in Tumor-Promoting Inflammation: Impairment of Macrophage Recruitment Evokes a Compensatory Neutrophil Response. Neoplasia (2015). doi:10.1593/neo.07871
69. Dongre A et al. Epithelial-to-mesenchymal transition contributes to immunosuppression in breast carcinomas. Cancer Res 77, 3982–3989 (2017). [PubMed: 28428275]
70. Lou Y et al. Epithelial-mesenchymal transition is associated with a distinct tumor microenvironment including elevation of inflammatory signals and multiple immune checkpoints in lung adenocarcinoma. Clin. Cancer Res 22, 3630–3642 (2016). [PubMed: 26851185]
71. Wellenstein MD et al. Loss of p53 triggers WNT-dependent systemic inflammation to drive breast cancer metastasis. Nature 2019 7 31. doi: 10.1038/s41586-019-1450-6.

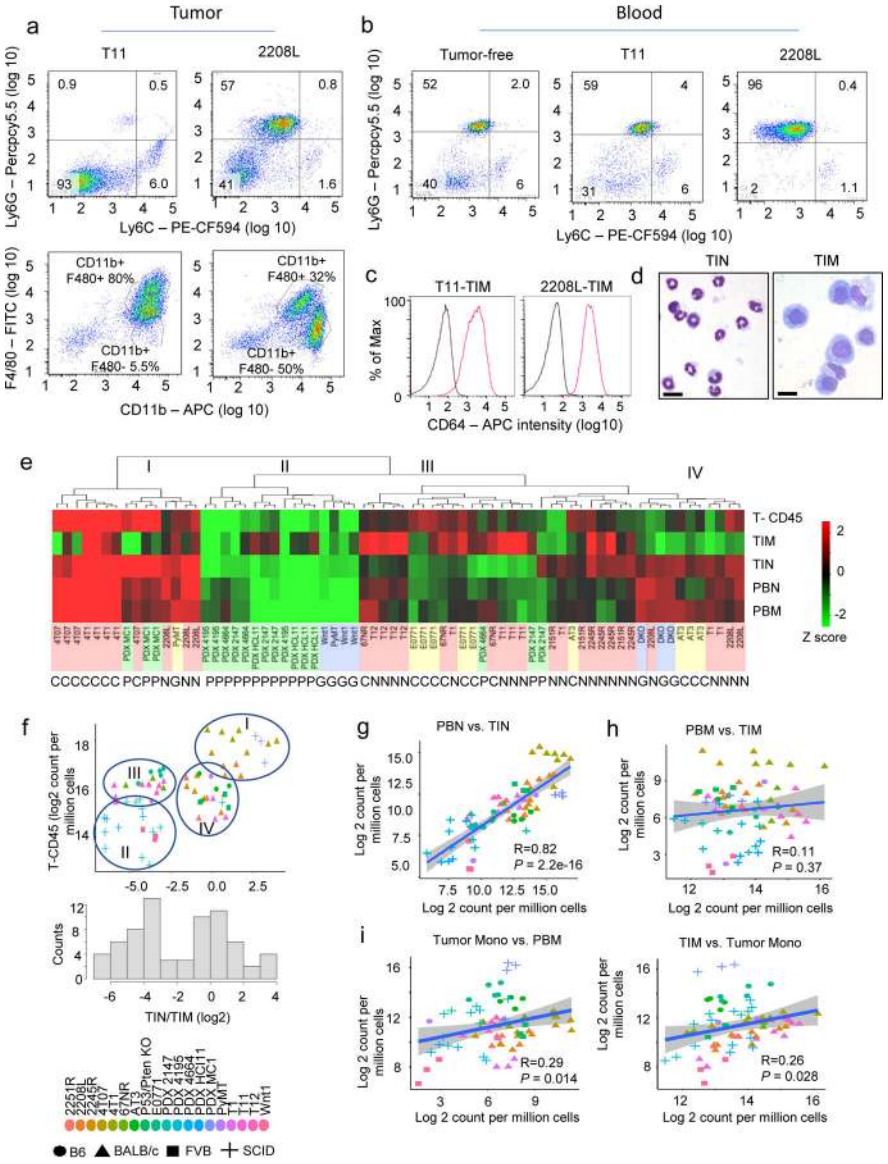

Figure 1. Diverse immune cell profiles in murine mammary tumor models.

(**a**) FACS analyses show dichotomous infiltration of $Ly6G^{+}Ly6C^{med\text{-}low}$ cells (neutrophils) and $CD11b^{+}F480^{+}$ cells (macrophages) in two representative tumor models. Plots are gated on $CD45^{+}CD11b^{+}$ cells (upper panel) and $CD45^{+}$ cells (lower panel).

(**b**) FACS analyses show variable systemic accumulation of $Ly6G^{+}$ $Ly6C^{med\text{-}low}$ cells (neutrophils) in peripheral blood of tumor-bearing mice. Plots are gated on CD45+ CD11b+ cells. For **a** and **b**, the experiments were repeated at least five times with similar results.

(**c**) CD64 staining of $CD45^{+}CD11b^{+}Ly6G^{TM}Ly6C^{TM}F4/80^{+}$ tumor-infiltrating macrophages (TIMs) shows positive signals (pink curve) as compared to unstained control (black curve) in T11 and 2208L model.

(**d**) Wright-Giemsa staining of purified $CD45^{+}$ $CD11b^{+}$ $Ly6G^{+}$ $Ly6C^{med\text{-}low}$ TINs (left) and $CD45^{+}CD11b^{+}Ly6C^{TM}Ly6G^{TM}F4/80^{+}$TIMs (right). Scale bar, 10 μm. For **c** and **d**, the experiments were done once.

(**e**) Heatmap shows unsupervised clustering of 19 breast tumor models (n=70 biologically independent animals) based on the frequency of total $CD45^+$ cells in tumors (T-CD45), TIM, TIN, peripheral blood $Ly6C^{high}$ monocytes (PBM), and peripheral blood neutrophils (PBN). All cell frequencies are normalized to total cells, log-transformed and then z-transformed. The genetic background of each model is encoded by a different color– pink: BALB/c; blue: FVB; yellow: C57BL/6; green: SCID/Beige. Experimental systems are indicated by letter code – C: cell lines; N: p53-null tumor (primary tissue); G: genetically engineered spontaneous tumors; and P: PDX models (human tumors in mouse).

(**f**) Upper panel: scatter plot of total $CD45^+$ cells against TIN/TIM ratios with the four clusters in (**e**) indicated by circles. Lower panel: histogram of log2-transformed TIN/TIM ratio of the tumor models/biological replicates shown in (**e**). n=70 biologically independent animals.

(**g-i**) Scatter plots show the correlations among indicated immune cells. Linear smoothed lines (blue lines) and confidence intervals (grey shades) are shown based on linear regression analyses. n=70 biologically independent animals. The Pearson correlation coefficients and corresponding P values based on two-sided *t*-tests.

For (**f-i**), genetic background and individual tumor models are indicated by distinct point shape and color, and are shown below (**f**).

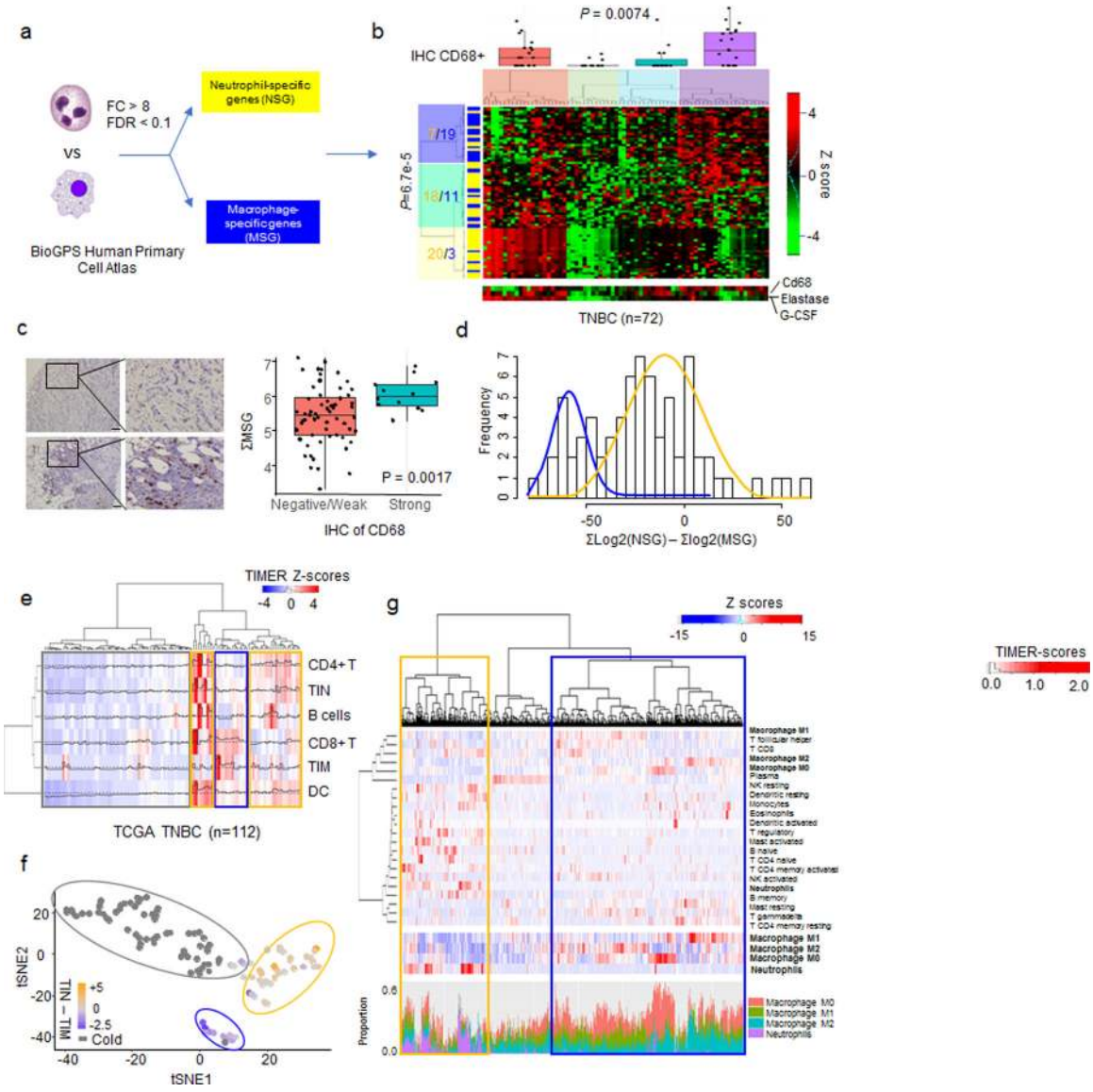

Figure 2. Myeloid cell profiles in human TNBC.

(**a**) Schematic shows the derivation of NSG and MSG based on Human Primary Cell Atlas of BioGPS. FC: fold change; FDR: false discovery rate

(**b**) Unsupervised clustering of a human TNBC nanostring dataset (n=72 patients) using MSG (blue) and NSG (yellow). Boxplots of CD68 IHC quantitation, and the gene expression levels of CD68, Elastase and G-CSF are indicated. The P value on the row-side was computed by two-sided Fisher's exact test. The P value along the column side with box plots was computed based on one-way ANOVA. The color scale indicates z-scores of log2-transformed, normalized counts.

(**c**) Left: IHC image of negative/weak (upper, representative of 60 patients) or strong (lower, representative of 12 patients) CD68 staining. Scale bar, 100 μm. Right: boxplots (defined in Methods) show normalized expression of MSG in tumors whose TMA sections exhibit negative or weak CD68 staining (positive cell count < 10, n=60 patients) or strong staining (> 10, n=12 patients). The P value is computed by two-sided *t*-tests with Welch correction.

(**d**) Histogram of log-transformed ratio of NSG over MSG. The approximated bimodal distribution is shown by solid lines.
(**e**) Unsupervised clustering of TIMER scores of six indicated immune cells in TNBC of TCGA dataset (n=112 patients) after z-transformation. Potential "cold", "NES", "MES" clusters are indicated by grey, yellow, and blue rectangle, respectively. DC: Dendritic cells.
(**f**) tSNE clustering of the same cohort of tumors (n=112 patients) as in (**e**). Tumors that are "cold" as determined in (**e**) are colored grey. Others are colored in gradient according to z-score difference between TIN and TIM. Clusters representing potential "NES" and "MES" subtypes are indicated by yellow, and blue circles, respectively.
(**g**) CIBERSORT output of TNBC was obtained from a previous study (n=973 patients)[47] and reanalyzed (upper panel). The contribution of macrophages and neutrophils to the clustering is highlighted in the middle panel. The predicted proportions of neutrophils and macrophages are displayed in stacked bars following the same order. yellow and blue rectangles indicate clusters of divergent ratios of neutrophils vs. macrophages, respectively.

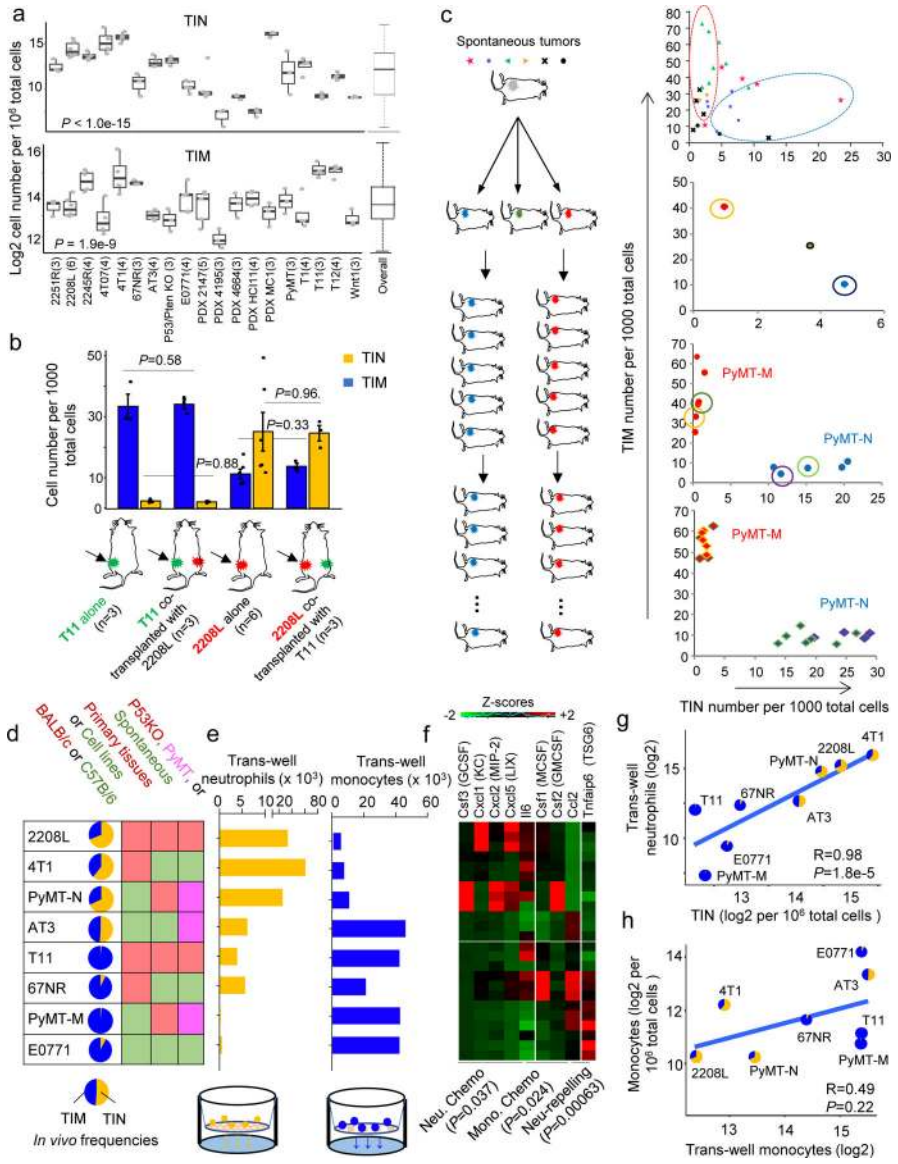

Figure 3. The TIN/TIM frequencies are relatively stable for individual tumor models.

(**a**) Box plots (defined in Methods) of TIN and TIM frequencies (relative to total cells) within individual model and across all models (rightmost plot). Each dot represents one tumor from a biologically independent animal, and the sample size of each model is indicated in parentheses. P value was computed by one-way ANOVA.

(**b**) Quantification of TIM and TIN in primary tumors. The sample size of each group is indicated in parentheses. Data are shown as mean ± S.D. P values were computed by two-sided *t*-tests, not adjusted for multiple comparisons.

(**c**) Development of MMTV-PyMT sublines that stably maintain divergent myeloid cell profiles. Experimental schematic is shown on the left and quantification of myeloid cells is on the right. Spontaneous tumors risen from the same animal are coded with same color and shape. Red or blue dotted circle indicates potential MES or NES tumors, respectively.

Tumors used for the next round of transplantation are solid-circled. Points of the resulting tumors are outlined with the same color as their parental tumor.

(**d**) TIM/TIN profiles in orthotopic tumors of eight models are presented as pie charts. Other characteristics are shown by colors as indicated by annotations above the table.

(**e**) Quantification of migrated neutrophils (left) and monocytes (right) toward tumor-conditioned medium.

(**f**) Heatmap shows the expression level of chemokines and cytokines known to regulate chemotaxis (chemo) of neutrophils (Neu.) and monocytes (Mono). Tnfaip6 is a neutrophil-repelling molecule. Z-scores are based on regularized log2-transformed RNA-seq data. Statistical difference of the sum of each group of genes between NES (n=4 biologically independent models: 2208L, 4T1, PyMT-N, and AT3) and MES (n=4 biologically independent models: T11, 67NR, PyMT-M, and E0771) is assessed by two-sided *t*-tests.

(**g** and **h**) Correlation between *in vitro* migration data and *in vivo* tumor infiltration data of neutrophils and monocytes (n=8 biologically independent models). The TIN/TIM profile of each model is indicated as a mini pie chart. Smoothed trend lines are shown. Pearson correlation coefficients and corresponding P value (by two-sided *t*-tests) are indicated.

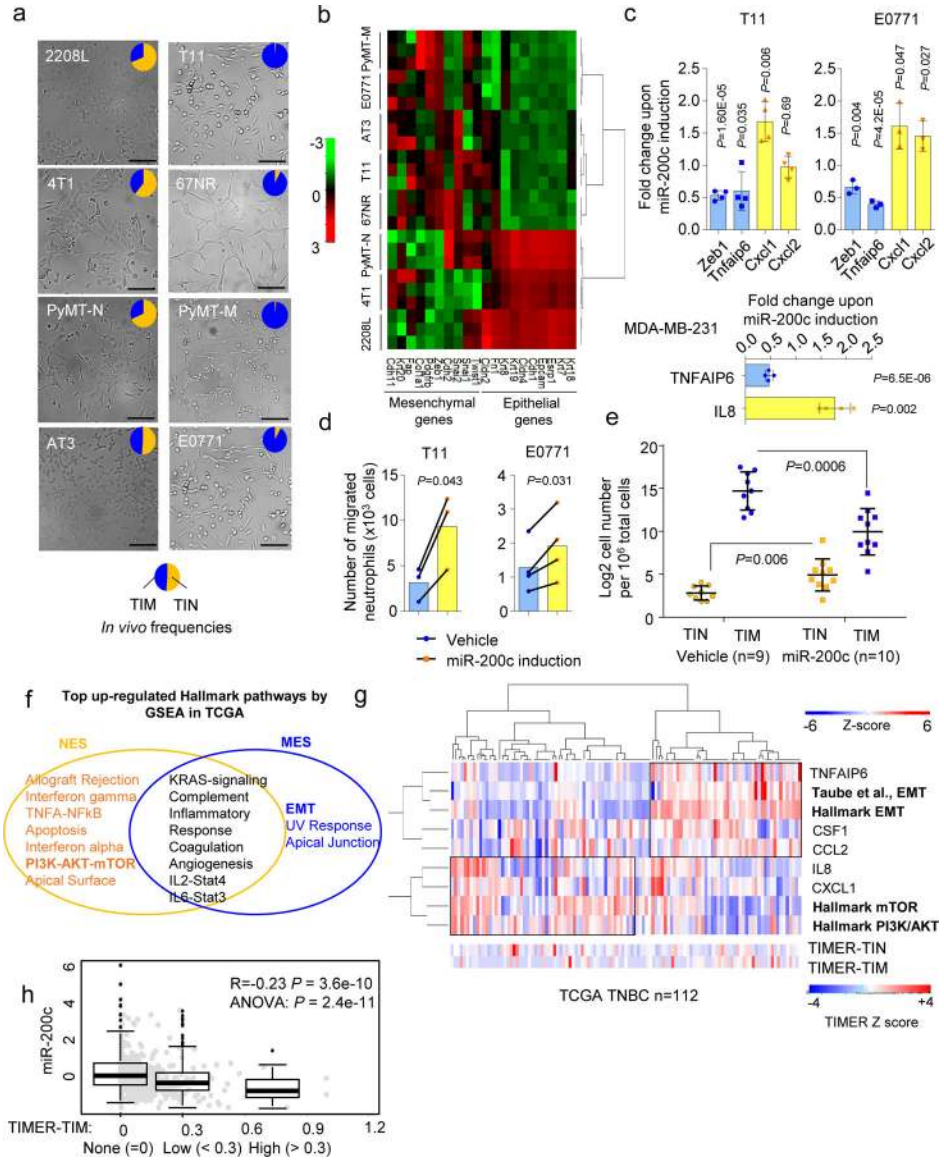

Figure 4. Perturbation of EMT tilts the balance between TIM and TIN.

(**a**) Cell morphology of eight tumor models in 2D culture. The pie charts are shown to indicate each model's *in vivo* TIM/TIN profiles. Scale bars, 100 μm.

(**b**) Heatmap shows the expression level of a panel of EMT-related genes across the eight models (each in technical triplicate). Color scale indicates Z-scores of regularized log-transformed data across columns.

(**c**) Relative expression of indicated genes in T11 (n=4), E0771 (n=3) and MDA-MB-231 (n=4) models upon miR-200c induction with doxycycline. Data are shown as mean ± S.D. P values was determined by two-sided *t*-tests.

(**d**) Quantification of neutrophil migration toward tumor-conditioned medium of T11 (n=3) and E0771 (n=4) cell line upon miR-200c induction with doxycycline. Bar graph represents the mean value of biological replicates. P values were determined by paired two-sided *t*-tests.

For **(c)** and **(d)**, n values indicate numbers of independent experiments.

(**e**) Quantification of TIM and TIN in orthotopic T11 tumors with or without miR-200c induction. Data are shown as mean ± S.D. P value was determined by two-sided Student's *t*-tests.

(**f**) Venn diagram shows the Hallmark Pathways associated with TIM and TIN frequencies in TCGA TNBC (n=112 patients) gauged by TIMER using GSEA. Significant pathways (FDR < 0.05 empirically determined by random permutations) are shown.

(**g**) Heatmap shows unsupervised hierarchical clustering of indicated genes and GSVA scores of indicated pathways (in bold) on TNBC of TCGA dataset. TIMER scores of TIN and TIM are shown on a separate scale after z-transformation. Two EMT-related gene sets (Taube et al.[55], and Hallmark EMT) and two mTOR pathway gene sets (Hallmark mTOR and Hallmark PI3K/AKT) are examined.

(**h**) Negative correlation between TIM TIMER scores (TIMER-TIM) and miR-200c expression in TCGA TNBC dataset (n=112 patients). Both scatter plots (grey dots) and boxplots (defined in Methods) are shown to treat TIMER-TIM as continuous and categorical variables (cutoffs indicated), respectively. A two-sided *t*-test (for the Pearson correlation coefficient) and one-way ANOVA are applied to compute P values.

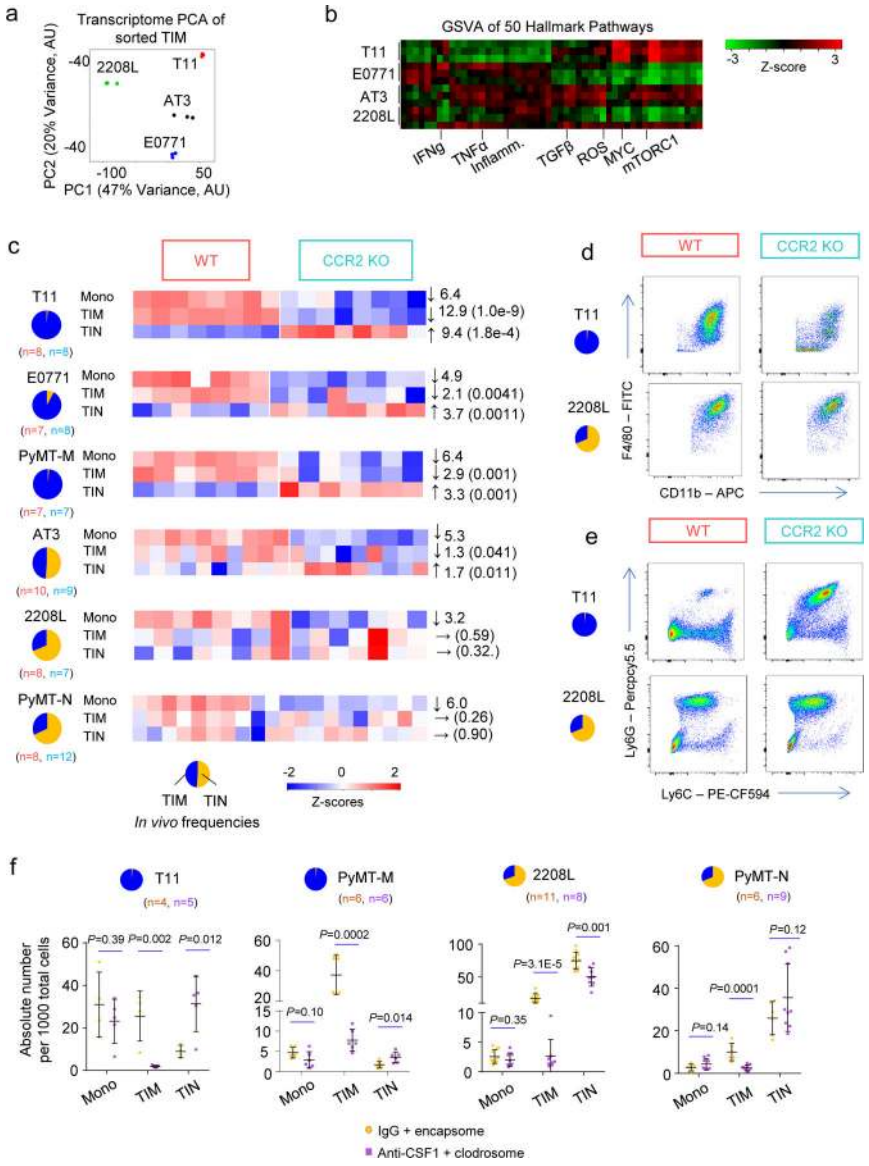

Figure 5. Inter-tumoral heterogeneity of TIMs and inverse change of TINs upon TIM depletion.

(**a**) Principle component analysis (PCA) of TIMs of four tumor models (n=3 biologically independent samples for each model).

(**b**) Heatmap shows unsupervised clustering of TIMs purified from four tumor models (n=3 biologically independent samples for each model) using GSVA of the 50 Hallmark Pathways from MSigDB. Pathways related to immunosuppressive or immunostimulatory activities are shown. The heatmap with complete pathway annotations is shown in Supplementary Fig. 5a.

(**c**) Heatmaps show the impact of CCR2 KO-mediated Ly6C high monocyte (Mono) depletion on the frequency of TIM and TIN in indicated tumor models. Number in parentheses show the specific n values of biologically independent mice per group denoted by different color. The absolute cell numbers were quantified by flow cytometry. Arrows to the right of the heatmaps show the direction of changes. Numbers beside the arrows indicate

fold changes of immune cell infiltration in CCR2 KO compared to wild type (WT). Numbers in parentheses indicate *P* values computed by two-sided *t*-tests.

(**d**) Example FACS plots show alteration of TIMs ($CD11b^{+}$ $Ly6C^{™}$ $Ly6C^{™}$ $F4/80^{+}$) in WT and CCR2 KO hosts bearing T11 and 2208L tumors as representatives of MES and NES, respectively.

(**e**) Example FACS plots show alteration of TINs ($CD11b^{+}$ $Ly6G^{+}$ $Ly6C^{med\text{-}low}$) in WT and CCR2 KO hosts bearing T11 and 2208L tumors as representatives of MES and NES, respectively. For **d** and **e**, the results are representative of at least eight biologically independent animals.

(**f**) Quantification of tumor-infiltrating monocytes (Mono), TIM, and TIN in indicated tumor models upon treatment of anti-CSF1 + clodrosome. Numbers in parentheses show the specific n values of biologically independent mice per group denoted by different color. Data are shown as mean ± S.D. P values were determined by two-sided *t*-test.

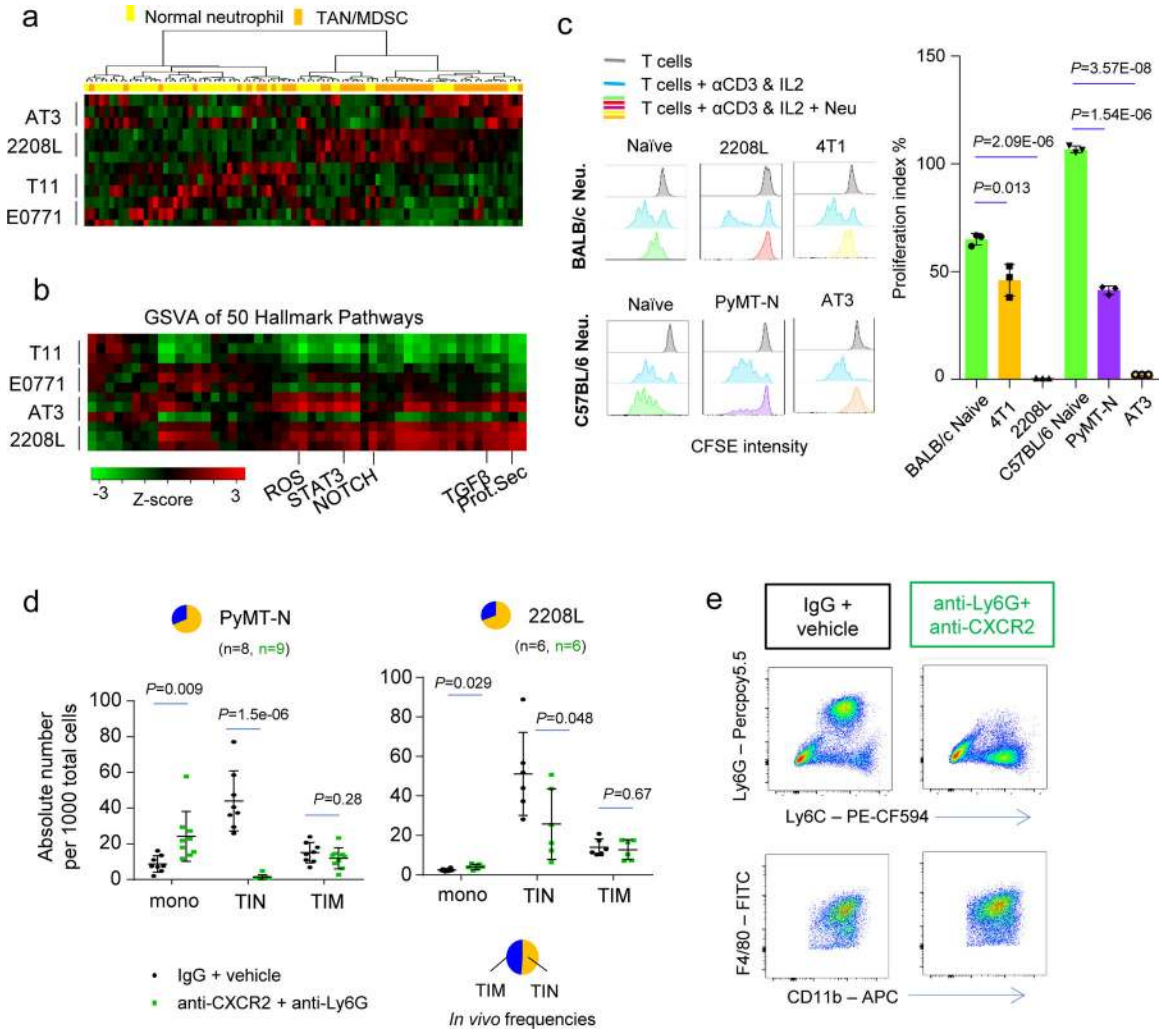

Figure 6. TINs in NES tumors express multiple immunosuppressive pathways, and negatively regulate Ly6C+ monocyte recruitment.

(**a**) Heatmap shows unsupervised hierarchical clustering of TINs purified from four tumor models (n=3 biologically independent samples for each model) using gene characteristic of normal neutrophils or TANs and/or MDSCs as published by Fridlender et al., 2012[59].

(**b**) Heatmap shows unsupervised clustering of TINs of four tumor models (n=3 biologically independent samples for each model) using GSVA of the 50 Hallmark Pathways from MSigDB. Pathways related to immunosuppressive activities are shown. The heatmap with all pathway annotated is shown in Supplementary Fig. 6a.

(**c**) *In vitro* immunosuppression assay by co-culturing bone marrow neutrophils from indicated NES tumor-bearing animals and splenic T cells. Proliferation of T cells was determined based on CFSE intensity as measured by FACS. A left-shift of CFSE intensity histogram indicates dilution of signals by proliferation. Data are shown as mean ± S.D. of three biological replicates (neutrophils from three different mice). P values were determined by two-sided *t*-tests. Neu.: neutrophil.

(**d**) Quantification of monocytes, TIN and TIM in NES tumors (PyMT-N and 2208L) upon treatment of anti-CXCR2 + anti-Ly6G. Number in parentheses show the specific n values of

biologically independent mice per group denoted by different color. Data are shown as mean ± S.D. P values were computed by two-sided Student's *t*-tests.

(**e**) Example FACS plots show alteration of TINs ($CD11b^{+}$ $Ly6G^{+}$ $Ly6C^{med\text{-}low}$), monocytes ($CD11b^{+}$ $Ly6G^{TM}Ly6C^{+}$), TIMs ($CD11b^{+}$ $Ly6G^{TM}$ $Ly6C^{TM}$ $F4/80^{+}$) in hosts bearing PyMT-N tumor (NES) treated with anti-Ly6G + anti-CXCR2 or IgG control. The results are representative of at least five biologically independent animals.

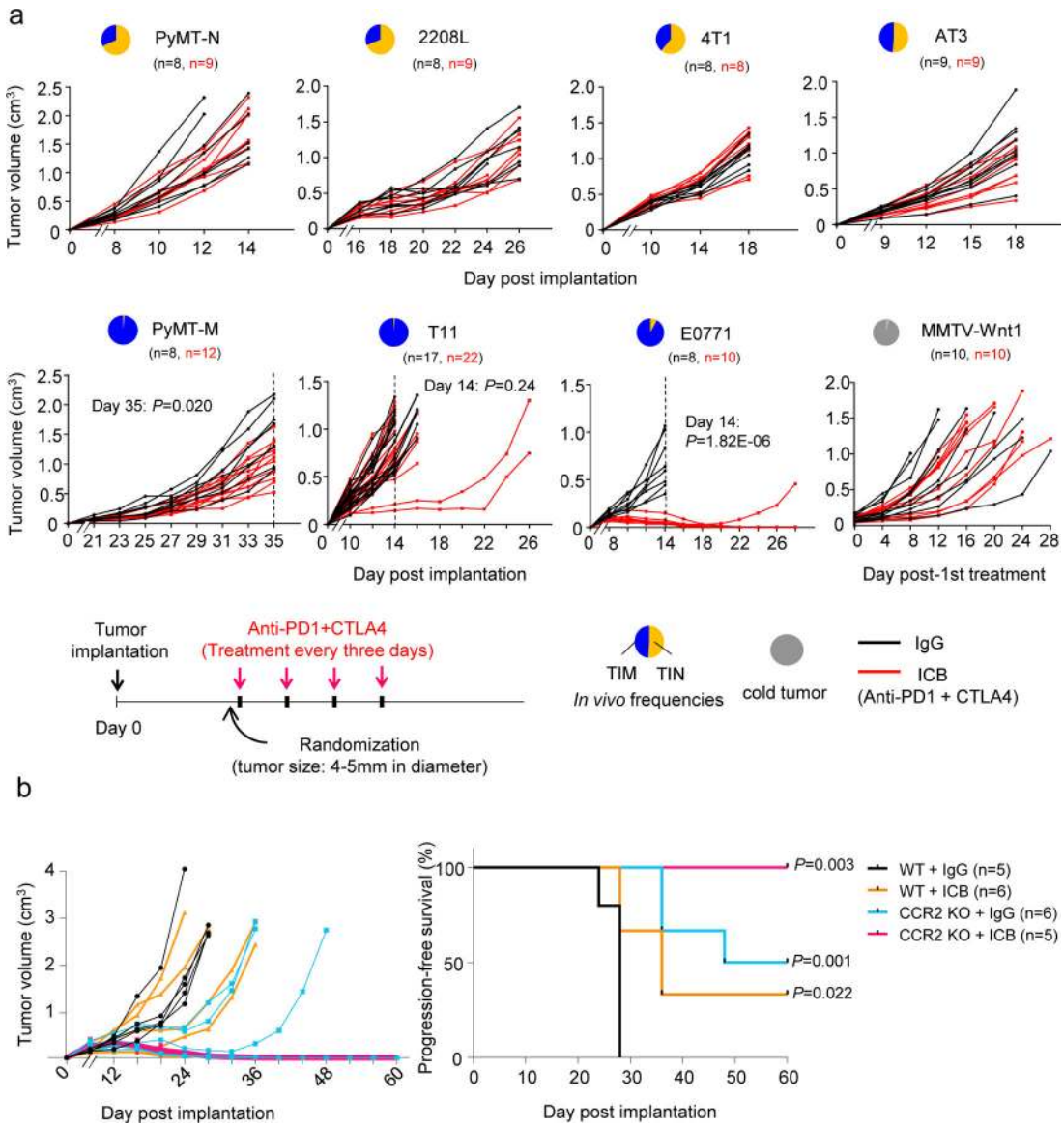

Figure 7. Heightened accumulation of immunosuppressive TINs or gMDSCs is associated with de novo resistance to ICB.

(**a**) Tumor growth curves show responses of indicated tumor models to ICB therapy (anti-PD1+anti-CTLA4). A treatment schematic is shown below the growth curves. Number in parentheses show the specific n values of biologically independent mice per group denoted by different color. Dotted lines indicate the time point at which tumor sizes were compared between control and treatment groups. P value was computed by two-sided *t*-test.

(**b**) Left: growth curves of T11 tumor in wild type (WT) or CCR2 knockout (CCR2 KO) mice with or without treatment of ICB (anti-PD1+anti-CTLA4). Right: Kaplan-Meier curves show the progression-free survival of the animals in four groups. Number in parentheses show the specific n values of biologically independent mice. P value was determined by two-sided log rank test, comparing each experimental group to WT + IgG control group.

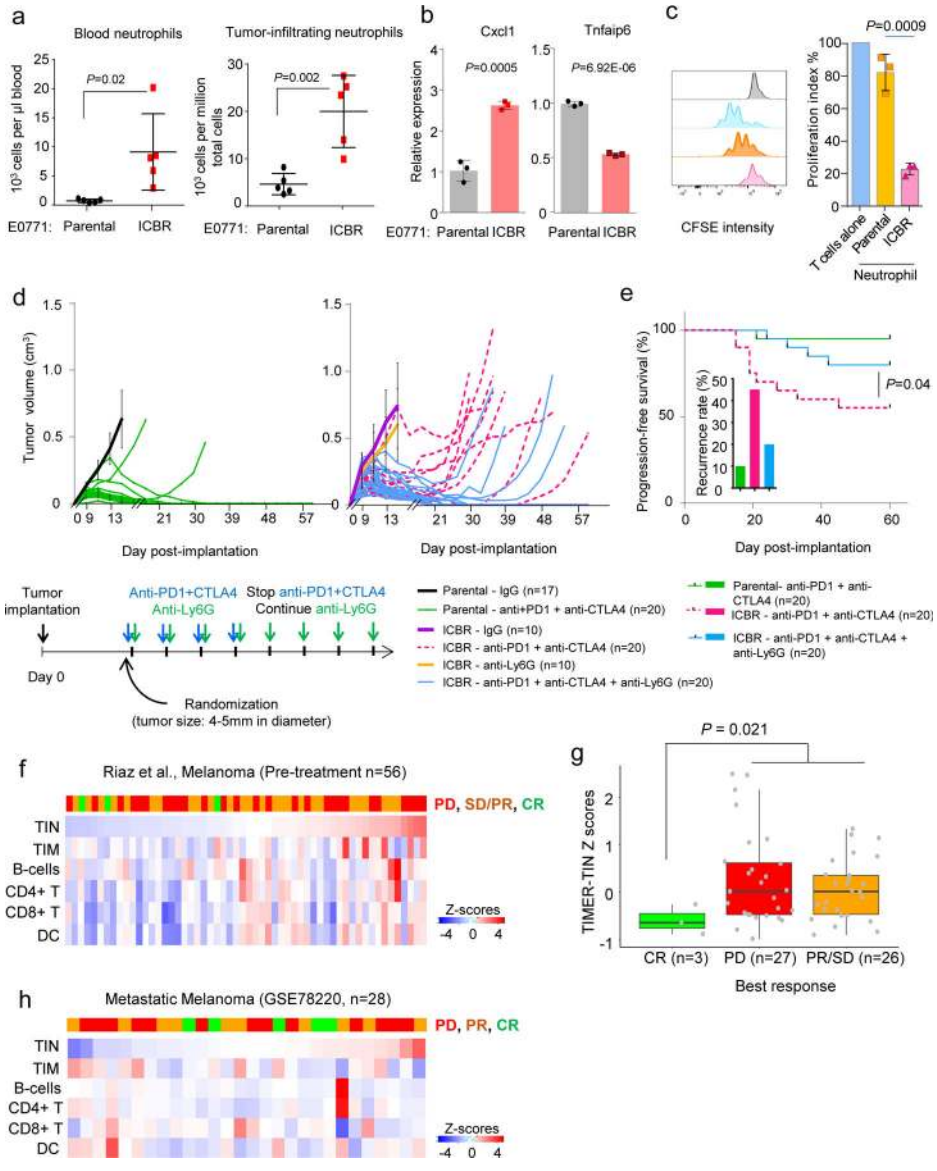

Figure 8. TINs mediate acquired resistance to ICB.

(**a**) Quantification of peripheral blood neutrophils and TINs in animals transplanted with parental (n=5) or recurrent (ICBR, n=5) E0771 tumor. Data are shown as mean ± S.D. P value was determined by a two-sided *t*-test.

(**b**) Relative expression of indicated genes in parental (n=3) and ICBR (n=3) E0771 cell lines. Data are shown as mean ± S.D. P value was determined by a two-sided *t*-test.

(**c**) *In vitro* immunosuppression assay by co-culturing bone marrow neutrophils from parental and ICBR E0771 tumor-bearing animals and splenic T cells. T cell proliferation was determined based by CFSE intensity as measured by FACS. Data are shown as mean ± S.D. of three biological replicates (neutrophils from three different mice). P value was computed using two-sided *t*-tests.

(**d**) Therapeutic responses of parental and ICBR E0771 tumors to ICB (anti-PD1 + anti-CTLA4) and/or neutrophil depletion (anti-Ly6G). A treatment schematic is shown below the

growth curves. Recurrence rate post-ICB is shown on the right. Because experimental groups without ICB never regressed (Parental IgG, ICBR IgG and ICBR anti-Ly6G), they were not further analyzed for recurrence rate or progression-free survival. Sample size of each group is provided in parentheses. Growth curves of Parental-IgG, ICBR-IgG, ICBR-anti-Ly6G groups are homogeneous, and therefore, are summarized as mean ± S.D. at each time point.

(**e**) Kaplan-Meier curves show the progression-free survival of parental or ICBR E0771 tumor-bearing animals subjected to either ICB or ICB+anti-Ly6G. P value was determined by two-sided log likelihood test. Recurrence rate post-ICB is shown as bar graphs under the curves.

(**f**) Heatmap shows the TIMER scores of indicated immune cells in a metastatic melanoma dataset [66]. Red/orange/green bars indicate progressive diseases (PD), partial response (including stabilized diseases, PR/SD), and complete response (CR), respectively.

(**g**) Box plots (defined in Methods) of TIN scores in patients with different responses to nivolumab. Sample size of each group is indicated in parentheses. P value was determined by two-sided *t*-test.

(**h**) The same as (**f**) except for a different metastatic melanoma dataset [67].